Formation Flying SAR: analysis of imaging performance by Array Theory

Alfredo Renga, *Member IEEE*, Maria Daniela Graziano, and Antonio Moccia, *Senior Member, IEEE*

Abstract—**This paper analyzes the process of image synthesis for a Formation Flying Synthetic Aperture Radar (FF-SAR), which is a multistatic Synthetic Aperture Radar (SAR) based on a cluster of receiving-only satellites flying in a close formation, in the framework of the array theory. Indeed, the imaging properties of different close receivers, when analyzed as isolated items, are very similar and form the so-called common array. Moreover, the relative positions among the receivers implicitly define a physical array, referred to as spatial diversity array. FF-SAR imaging can be verified as a result of the spatial diversity array weighting the common array. Hence, different approaches to beamforming can be applied to the spatial diversity array to provide the FF-SAR with distinctive capabilities, such as coherent resolution enhancement and high-resolution wide-swath imaging. Simulation examples are discussed which confirm that array theory is a powerful tool to quickly and easily characterize FF-SAR imaging performance.**

Index Terms—**array theory, distributed arrays, Formation Flying SAR, High-Resolution Wide-Swath imaging, Multistatic SAR, spaceborne SAR, Synthetic Aperture Radar.**

I. INTRODUCTION

SPACEBORNE Synthetic Aperture Radar (SAR) remote sensing missions have been delivering operational products and services since the early 1990s. In the last decade, SAR satellites have grown in number, capability, and complexity, culminating with the realization of multi-satellite missions, such as COSMO-SkyMed [1] and Sentinel-1 [2] constellations and TanDEM-X formation [3]-[4]. An important trend in satellite remote sensing technology is also towards system miniaturization. Spaceborne SAR missions have been successfully deployed relying on very compact platforms, i.e. the Israeli TecSAR (300 kg launch mass) [5], the Indian RISAT-2 (300 kg launch mass) [6], and the Finnish ICEYE-X1 (70 kg launch mass) [7]. Despite the rapid technological advances that have characterized satellite SAR missions, miniaturization has been only obtained at the expense of performance parameters, like mission lifetime, orbit duty cycle, image resolution, ground coverage, interferometric revisit.

The term Formation Flying SAR (FF-SAR) is used in this paper to indicate a cluster of receiving-only satellites flying in a close formation. Each satellite collects the echoed signal emitted by the transmitter and scattered from the area of interest. These collected echoes are then coherently combined to enhance the overall system performance and the quality of the delivered products.

The authors are with the Department of Industrial Engineering, University of Naples "Federico II," 80125 Naples, Italy (e-mail: alfredo.renga@unina.it).

Thanks to passive operations, an FF-SAR achieves high performance through a series of very compact, low weight, platforms. So, the FF-SAR mission concept is naturally coupled with the use of small space platforms. As a consequence, the system overall cost is lower, the replacement of a failed satellite is easier and faster, and it is possible to gradually update on board technologies by incrementally replacing elements of the formation, which is generally an issue for large monolithic space systems. Indeed, small satellite missions offer the opportunity to rapidly and flexibly inject new technology developments in spaceborne solutions. Concerning this, a CubeSat train was recently proposed [8] for high resolution radar sounding and imaging of Antarctica. The formation includes 50 CubeSats. Formation design and Earth rotation are used to synthesize a large cross-track array. The coherent combination of radar echoes collected by each platform is thus expected to guarantee high cross-track resolution, which is difficult to achieve by single satellite radar sounding.

An FF-SAR represents a generalization of the conventional SAR principle [9]-[10], and of standard interferometric SAR (InSAR) techniques [11], towards a highly flexible system able to implement a wide range of different working modes. When both cross-track/radial and along-track separations are available, the coherent processing approach can be adaptively modified to improve the desired imaging feature to the current scene and to the observation requirements. In addition, the separations among the receivers can be changed during the mission to further improve the system capabilities. According to multistatic SAR literature [12], various multistatic configurations can be defined, including: fully-active systems, multi-monostatic, and semi-active systems. In this sense, the above-defined FF-SAR, if realized as a companion satellite mission [13], i.e. collecting echoes from a pre-existing monostatic SAR, can be also interpreted as a specific case of semi-active multistatic SAR. Safe formation flying operations [3],[14]-[15] and precise clock synchronization [12],[16]-[22] among the receivers are pre-requisites for FF-SAR implementation. Important capabilities in this ambit have already been successfully demonstrated by past bistatic SAR missions, like TanDEM-X mission [4], and more recently, in small satellite formation flying missions, like CanX-4&5 [18].

An FF-SAR can also operate as a multi-baseline single-pass interferometer. Such a configuration has been proposed to implement advanced InSAR techniques [12] like single-pass tomography and Ground Moving Target Indication (GMTI) or to complement the processing architectures of differential SAR interferometry (DInSAR) through repeated multi-baseline
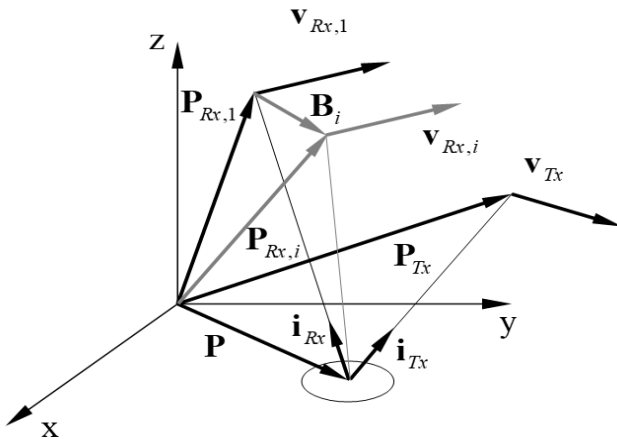
Fig. 1. FF-SAR geometry.

single-pass acquisitions. In this context, experimental results and methodologies are available [19]-[21].

The FF-SAR technique is analyzed in this paper from a different perspective. Indeed, the working principle of the FF-SAR is not new. Its theoretical foundation can be dated back to [22]. Moreover, demonstrations have been performed in previous spaceborne [23] systems. The present work is mainly focused on FF-SAR imaging features, that is on the derivation of an analytical model to be used for evaluation of FF-SAR imaging performance. This FF-SAR image, thanks to the spatial diversity of the collection geometry and the redundancy of the measurements, is characterized by enhanced properties with respect to the image that a single receiver of the formation can generate when operating as an isolated item. Some studies have already investigated this topic [24]-[26]. An imaging model based on the k-space method was discussed in [24] able to represent the Point Spread Function (PSF) for a system of cooperative multi-monostatic SARs. The present paper starts from this concept to introduce a model for representing the point target response of an FF-SAR and the key role played by the relative geometries between the transmitter and the available receivers. With specific reference to multiple formation flying receivers, most of the available results concern satellite formations with along-track only separations to apply High-Resolution Wide-Swath (HRWS) imaging, i.e. placing formation flying satellites as a multi-channel antenna in the along-track direction. An imaging model able to deal with both along-track and cross-track/vertical separations among the receivers is that proposed in [27]-[28]. The model originally introduced the concept of sensor vector to characterize the added value of the spatial diversity among the receivers with respect to standard SAR coordinates of frequency and time. A key tool of the model is the array theory that effectively measures the relative contributions and the importance of frequency, time, and spatial diversity to determine image performance. The principle shows similarity with the k-space method [24], in which a k-set is introduced with the PSF of the system computed as the Fourier Transform of the k-set. However, the array theory is best suited for analyzing the

effects of multistatic acquisitions on the imaging performance. The model of [27]-[28] assumes that the transmitter and receivers fly at the same velocity, so it can be applied to the case in which the transmitter is flying in a very close formation with the receivers. The range of applicability of this model is thus limited. It cannot be used to study upcoming mission concepts like SESAME [29], STEREOID [30], Multi-static HRWS [31], and, more in general, is not valid when a formation of receivers is realized to complement an already existing monostatic SAR mission, i.e. for the case of companion satellites [13], [32]-[33]. Indeed, performance enhancement made possible by FF-SAR is independent of the location of the transmitter, which can also be a mere illuminator, since FF-SAR does not need a monostatic SAR image to be exploited. This leads to even more exotic configurations, e.g. based on Geostationary transmitters [34]-[35] or Digital Video Broadcasting Terrestrial (DVB-T) opportunity illuminators [36].

The basic idea of this paper is that the imaging properties of all receivers, when analyzed as isolated items, are very similar and can be represented by a so-called common array pattern, i.e. receivers are in close formation. Moreover, the relative positions among the receivers implicitly define a physical array, referred to as the spatial diversity array. The combination of the common and the spatial diversity arrays by suitable beamforming techniques lead to the resulting FF-SAR image. The introduced approach is of quite general validity meaning that it can be applied to i) close satellite formations including both a monostatic SAR and a given number of receivers, as in [3],[27]; ii) companion satellite-like configurations, i.e. large satellite formations with a transmitter that is relatively far from a cluster of receivers, as in [29]-[33]; iii) formations of close receivers working with transmitters operating at completely different ranges of altitude and velocity, as in [34]-[37]. The main output of the proposed model is the FF-SAR point target response, from which general performance parameter [38], like resolution, Peak-to-Side-Lobe Ratio (PSLR), Integrated Side-lobe Ratio (ISLR), ambiguity levels, can be readily computed.

This paper is organized as follows. Section II presents the FF-SAR signal model introducing the main relevant parameters and operators. The interpretation of FF-SAR image synthesis in the framework of array theory is illustrated in Section III, where the concepts of common and spatial diversity array are formulated. Then, Section IV discusses the most prominent FF-SAR beamforming techniques allowing the system to achieve Coherent Resolution Enhancement (CRE), Signal-to-Noise Ratio (SNR) improvement, and HRWS imaging. The application of the developed methodology to some examples of satellite formations is described in Section V.

II. FF-SAR SIGNAL MODEL

A reference frame is defined in Figure 1, with the origin of coordinates located at the center of the scene to be imaged, and x-y as the local plane. Transmitter and receivers fly linear flight paths at constant velocity within the coherent processing interval. Transmitter position and velocity are indicated as $\mathbf{P}_{Tx}$

and $\mathbf{v}_{Tx}$, respectively, whereas the position vector of the ith receiver is $\mathbf{P}_{Rx,i}$ and its velocity is $\mathbf{v}_{Rx,i}$.

It worth noting that, differently from [27]-[28],

$$\mathbf{v}_{Tx} \neq \mathbf{v}_{Rx,i} \qquad i = 1,...,N \tag{1}$$

where N is the number of receivers. So, the transmitter moves along a trajectory which is different from those of the receivers. Nonetheless, since coherent combination among the data collected by each receiver must be allowed, the receivers are assumed to fly as a satellite formation

$$\frac{\left|\mathbf{v}_{Rx,i} - \mathbf{v}_{Rx,k}\right|}{\left|\mathbf{v}_{Rx,k}\right|} << 1 \qquad \forall i,k \tag{2}$$

where $|\ |$ is the Euclidean norm. According to Eq. (2), velocity variations among the receivers within the coherent processing interval can be neglected, that is $\mathbf{v}_{Rx,i} \cong \mathbf{v}_{Rx}$, $\forall i$.

Based on the start-stop approximation [38]-[39], the raw bistatic signal at the ith receiver from a stationary point target located in $\mathbf{P}$ can be formulated

$$S_{Rx}(\mathbf{P},u,t,i) = \gamma(\mathbf{P})G_{Tx}(t,\mathbf{P}) \cdot G_{Rx}(t,\mathbf{P}) \cdot$$
$$\exp\left\{j\left[\pi\alpha\left[u - \frac{R_{Tx}(t) + R_{Rx,i}(t)}{c}\right]^2\right]\right\} \cdot$$
$$\exp\left\{-j\frac{2\pi f_c}{c}\left[R_{Tx}(t) + R_{Rx,i}(t)\right]\right\} \cdot \tag{3}$$
$$rect\left(\frac{u - \frac{R_{Tx}(t) + R_{Rx,i}(t)}{c}}{\tau_p}\right)$$
$$i = 1,...,N$$

where u is the fast-time, t is the slow time, γ is the complex reflection coefficient of the target, G_{Tx} and G_{Rx} are respectively, transmitting (Tx) and receiving (Rx) antenna gains in the direction of the targets, j is the imaginary unit, α is the chirp rate, that is the ratio between signal bandwidth and the pulse length τ_p, c is the speed of light, and f_c is the carrier frequency. The model of Eq. (3) is the same as the standard one used for monostatic SAR [38], in which the monostatic range history is replaced by the bistatic one, i.e. $R_{Tx}(t) = \left|\mathbf{P}_{Tx}(t) - \mathbf{P}\right|$ and $R_{Rx,i}(t) = \left|\mathbf{P}_{Rx,i}(t) - \mathbf{P}\right|$. The fast-time Fourier transform of the raw bistatic signal can be computed as in [38] by the Principle of Stationary Phase, thus yielding

$$S_{Rx}(\mathbf{P},f,t,i) = A_1\gamma(\mathbf{P})G_{Tx}(t,\mathbf{P}) \cdot G_{Rx}(t,\mathbf{P}) \cdot$$
$$rect\left(\frac{f}{\alpha\tau_p}\right) \cdot$$
$$\exp\left(-j\frac{2\pi(f_c + f)}{c}\left(R_{Tx}(t) + R_{Rx,i}(t)\right)\right) \cdot \tag{4}$$
$$\exp\left(-j\frac{\pi f^2}{\alpha}\right)$$
$$i = 1,...,N$$

where A_1 is a constant and f is the fast-time-frequency. A suitable approach to interpret FF-SAR imaging is by the basic array theory, that is analyzing the resulting radiation pattern [40] of the array represented (virtually) by the phase contributions of the signals collected by each receiver according to Eq. (4). No straightforward application of this idea can be performed as long as the phase model is not reformulated more conveniently. Required derivation is similar to the one discussed in [27]-[28] and it is herein presented.

Without loss of generality, one can assume the first receiver as the reference receiver. So, the baseline vector, $\mathbf{B}$, can be introduced, representing the vector from the position of the reference receiver, $\mathbf{P}_{Rx}$, to the generic one of the formation

$$\mathbf{B} = \mathbf{P}_{Rx,i} - \mathbf{P}_{Rx} = \begin{bmatrix} B_x & B_y & B_z \end{bmatrix}^T \tag{5}$$

and the superscript T indicates the transpose operation. According to Eqs. (4)-(5), the phase is a function of 5 parameters which can be grouped in a single vector

$$\mathbf{s} = \begin{bmatrix} B_x & B_y & B_z & f & t \end{bmatrix}^T \tag{6}$$

referred to as sensor vector in [27]-[28]. Eqs. (4)-(6) states that each receiver observes the scene as a function of frequency (i.e. range or fast time) and slow time (i.e. azimuth) as in standard SAR, but those collections are performed from different relative positions $\mathbf{B}$, which introduce a spatial diversity in the data, affecting the phase of collected signals too. Therefore, a useful representation of the phase can be obtained by two consecutive first-order Taylor series expansion, the first one as a function of the parameters, $\mathbf{s}$, and the second one as a function of target location, $\mathbf{P}$. The first series expansion is performed around

$$\tilde{\mathbf{s}} = \begin{bmatrix} 0 & 0 & 0 & 0 & 0 \end{bmatrix}^T \tag{7}$$

and yields

$$\Psi(\mathbf{P},\mathbf{s}) \cong \Psi(\mathbf{P},\tilde{\mathbf{s}}) + \left(\nabla_{\mathbf{s}}\Psi\big|_{\mathbf{P},\tilde{\mathbf{s}}}\right)^T \Delta\mathbf{s} \tag{8}$$

where $\nabla_{\mathbf{s}}$ indicates the gradient operator with respect to sensor

parameters. The phase derivative with respect to the frequency is proportional to the time delay

$$\left.\frac{\partial \Psi}{\partial f}\right|_{\mathbf{P},\tilde{\mathbf{s}}} = -\frac{2\pi}{c}\Big[\big|\mathbf{P}_{Tx}(0)-\mathbf{P}\big|+\big|\mathbf{P}_{Rx}(0)-\mathbf{P}\big|\Big] = 2\pi\,\tau(\mathbf{P},\tilde{\mathbf{s}}) \quad (9)$$

whereas the derivative with respect to time is related to the Doppler frequency

$$\left.\frac{\partial \Psi}{\partial t}\right|_{\mathbf{P},\tilde{\mathbf{s}}} = -\frac{2\pi}{\lambda}\Big[\mathbf{v}_{Tx}^{T}\mathbf{i}_{Tx}(\mathbf{P},\tilde{\mathbf{s}})+\mathbf{v}_{Rx}^{T}\mathbf{i}_{Rx}(\mathbf{P},\tilde{\mathbf{s}})\Big] = 2\pi f_{D}(\mathbf{P},\tilde{\mathbf{s}}) \quad (10)$$

with $\mathbf{i}_{Tx}$ and $\mathbf{i}_{Rx}$ as the unit vectors from $\mathbf{P}$ to the transmitter and to the reference receiver, respectively (see Fig. 1), and λ as the carrier wavelength. Finally, the derivatives with respect to baseline components are

$$\left.\frac{\partial \Psi}{\partial \mathbf{B}}\right|_{\mathbf{P},\tilde{\mathbf{s}}} = -\frac{2\pi}{\lambda}\mathbf{i}_{Rx}^{T}(\mathbf{P},\tilde{\mathbf{s}}) \quad (11)$$

$$\Delta\mathbf{P}_{xy} = \begin{bmatrix} P_{x}-P_{x_0} & P_{y}-P_{y_0} \end{bmatrix}^{T} \quad (14)$$

and $\nabla_{\mathbf{P}} = \begin{bmatrix} \partial/\partial P_{x} & \partial/\partial P_{y} \end{bmatrix}^{T}$ is the gradient operator with respect to ground coordinates.

Analytic formulas for the gradient of the time delay and of the Doppler frequency can be found in bistatic SAR literature [35],[41]-[43]

$$\left.\nabla_{\mathbf{P}}\tau(\mathbf{P},\tilde{\mathbf{s}})\right|_{\tilde{\mathbf{P}},\tilde{\mathbf{s}}} = \frac{1}{c}\Big[\mathbf{i}_{Tx}(\tilde{\mathbf{P}},\tilde{\mathbf{s}})+\mathbf{i}_{Rx}(\tilde{\mathbf{P}},\tilde{\mathbf{s}})\Big]$$

$$\left.\nabla_{\mathbf{P}}f_{D}\right|_{\tilde{\mathbf{P}},\tilde{\mathbf{s}}} = \frac{1}{\lambda}\Bigg\{\frac{1}{\big|\mathbf{P}_{Tx}(0)-\tilde{\mathbf{P}}\big|}\Big[\mathbf{v}_{Tx}-\big(\mathbf{v}_{Tx}^{T}\mathbf{i}_{Tx}(\tilde{\mathbf{P}},\tilde{\mathbf{s}})\big)\mathbf{i}_{Tx}(\tilde{\mathbf{P}},\tilde{\mathbf{s}})\Big]+ \quad (15)$$
$$+\frac{1}{\big|\mathbf{P}_{Rx}(0)-\tilde{\mathbf{P}}\big|}\Big[\mathbf{v}_{Rx}-\big(\mathbf{v}_{Rx}^{T}\mathbf{i}_{Rx}(\tilde{\mathbf{P}},\tilde{\mathbf{s}})\big)\mathbf{i}_{Rx}(\tilde{\mathbf{P}},\tilde{\mathbf{s}})\Big]\Bigg\}$$

Moreover, after proper algebra, one can verify that

$$\left.\nabla_{\mathbf{P}}\mathbf{i}_{Rx}^{T}(\mathbf{P},\tilde{\mathbf{s}})\right|_{\tilde{\mathbf{P}},\tilde{\mathbf{s}}} = \begin{bmatrix} -\dfrac{1}{\big|\mathbf{P}_{Rx}(0)-\tilde{\mathbf{P}}\big|}+\dfrac{\big(P_{Rx,x}(0)-P_{x_0}\big)^{2}}{\big|\mathbf{P}_{Rx}(0)-\tilde{\mathbf{P}}\big|^{3}} & \dfrac{\big(P_{Rx,x}(0)-P_{x_0}\big)\big(P_{Rx,y}(0)-P_{y_0}\big)}{\big|\mathbf{P}_{Rx}(0)-\tilde{\mathbf{P}}\big|^{3}} & \dfrac{P_{Rx,z}(0)\big(P_{Rx,x}(0)-P_{x_0}\big)}{\big|\mathbf{P}_{Rx}(0)-\tilde{\mathbf{P}}\big|^{3}} \\[4mm] \dfrac{\big(P_{Rx,x}(0)-P_{x_0}\big)\big(P_{Rx,y}(0)-P_{y_0}\big)}{\big|\mathbf{P}_{Rx}(0)-\tilde{\mathbf{P}}\big|^{3}} & -\dfrac{1}{\big|\mathbf{P}_{Rx}(0)-\tilde{\mathbf{P}}\big|}+\dfrac{\big(P_{Rx,y}(t)-P_{y_0}\big)^{2}}{\big|\mathbf{P}_{Rx}(0)-\tilde{\mathbf{P}}\big|^{3}} & \dfrac{P_{Rx,z}(0)\big(P_{Rx,y}(0)-P_{y_0}\big)}{\big|\mathbf{P}_{Rx}(t)-\tilde{\mathbf{P}}\big|^{3}} \end{bmatrix} \quad (16)$$

So, following the first Taylor series expansion and neglecting the constant phase term $\Psi(\mathbf{P},\tilde{\mathbf{s}})$, the phase is

$$\Psi(\mathbf{P},\mathbf{s}) \cong -\frac{2\pi}{\lambda}\mathbf{i}_{Rx}^{T}(\mathbf{P},\tilde{\mathbf{s}})\mathbf{B}+2\pi\tau(\mathbf{P},\tilde{\mathbf{s}})f+2\pi f_{D}(\mathbf{P},\tilde{\mathbf{s}})t \quad (12)$$

Then, a second Taylor series expansion must be used to calculate the variation of phase gradients as a function of ground target location, that is

$$\mathbf{i}_{Rx}^{T}(\mathbf{P},\tilde{\mathbf{s}}) \cong \mathbf{i}_{Rx}^{T}(\tilde{\mathbf{P}},\tilde{\mathbf{s}})+\Delta\mathbf{P}_{xy}^{T}\nabla_{\mathbf{P}}\mathbf{i}_{Rx}^{T}(\mathbf{P},\tilde{\mathbf{s}})\big|_{\tilde{\mathbf{P}},\tilde{\mathbf{s}}}$$

$$\tau(\mathbf{P},\tilde{\mathbf{s}}) \cong \tau(\tilde{\mathbf{P}},\tilde{\mathbf{s}})+\Delta\mathbf{P}_{xy}^{T}\nabla_{\mathbf{P}}\tau(\mathbf{P},\tilde{\mathbf{s}})\big|_{\tilde{\mathbf{P}},\tilde{\mathbf{s}}} \quad (13)$$

$$f_{D}(\mathbf{P},\tilde{\mathbf{s}}) \cong f_{D}(\tilde{\mathbf{P}},\tilde{\mathbf{s}})+\Delta\mathbf{P}_{xy}^{T}\nabla_{\mathbf{P}}f_{D}(\mathbf{P},\tilde{\mathbf{s}})\big|_{\tilde{\mathbf{P}},\tilde{\mathbf{s}}}$$

where $\tilde{\mathbf{P}} = \begin{bmatrix} P_{x0} & P_{y0} & 0 \end{bmatrix}^{T}$ is a ground reference location, $\Delta\mathbf{P}_{xy}$ is a ground displacement with respect to that location

As a result of the second Taylor expansion, the phase becomes

$$\Psi(\mathbf{P},\mathbf{s}) \cong -\frac{2\pi}{\lambda}\mathbf{i}_{Rx}^{T}(\tilde{\mathbf{P}},\tilde{\mathbf{s}})\mathbf{B}+2\pi\tau(\tilde{\mathbf{P}},\tilde{\mathbf{s}})f+2\pi f_{D}(\tilde{\mathbf{P}},\tilde{\mathbf{s}})t$$
$$-\frac{2\pi}{\lambda}\Delta\mathbf{P}_{xy}^{T}\nabla_{\mathbf{P}}\mathbf{i}_{Rx}^{T}(\mathbf{P},\tilde{\mathbf{s}})\big|_{\tilde{\mathbf{P}},\tilde{\mathbf{s}}}\mathbf{B}+$$
$$2\pi\Delta\mathbf{P}_{xy}^{T}\nabla_{\mathbf{P}}\tau(\mathbf{P},\tilde{\mathbf{s}})\big|_{\tilde{\mathbf{P}},\tilde{\mathbf{s}}}f+ \quad (17)$$
$$2\pi\Delta\mathbf{P}_{xy}^{T}\nabla_{\mathbf{P}}f_{D}(\mathbf{P},\tilde{\mathbf{s}})\big|_{\tilde{\mathbf{P}},\tilde{\mathbf{s}}}t$$

and if one defines

$$\Delta\mathbf{s} = \begin{bmatrix} B_{x} & B_{y} & B_{z} & f & t \end{bmatrix}^{T}$$

$$\mathbf{k}(\tilde{\mathbf{P}},\tilde{\mathbf{s}}) = \begin{bmatrix} -\dfrac{2\pi}{\lambda}\mathbf{i}_{Rx}^{T}(\tilde{\mathbf{P}},\tilde{\mathbf{s}}) & 2\pi\tau(\tilde{\mathbf{P}},\tilde{\mathbf{s}}) & 2\pi f_{D}(\tilde{\mathbf{P}},\tilde{\mathbf{s}}) \end{bmatrix}^{T} \in \mathbb{R}^{5\times 1} \quad (18)$$

$$\Lambda_{s} = \begin{bmatrix} -\dfrac{2\pi}{\lambda}\nabla_{\mathbf{P}}\mathbf{i}_{Rx}^{T}(\mathbf{P},\tilde{\mathbf{s}})\big|_{\tilde{\mathbf{P}},\tilde{\mathbf{s}}} & 2\pi\nabla_{\mathbf{P}}\tau(\mathbf{P},\tilde{\mathbf{s}})\big|_{\tilde{\mathbf{P}},\tilde{\mathbf{s}}} & 2\pi\nabla_{\mathbf{P}}f_{D}(\mathbf{P},\tilde{\mathbf{s}})\big|_{\tilde{\mathbf{P}},\tilde{\mathbf{s}}} \end{bmatrix} \in \mathbb{R}^{2\times 5}$$

the phase can be rewritten in a more compact form as

$$\Psi(\mathbf{P},\mathbf{s}) \cong \mathbf{k}^T\left(\tilde{\mathbf{P}},\tilde{\mathbf{s}}\right)\Delta\mathbf{s} + \Delta\mathbf{P}_{xy}^T\Lambda_s\Delta\mathbf{s} \qquad (19)$$

Eq. (19) is of more general validity than the phase model of [27]-[28] since an analytic model for Λ_s has been derived here for a generic FF-SAR geometry and it represents its generalization to the case of N satellite receivers flying in a close formation and sharing the same transmitter which operates, in general, on a different and independent trajectory. In fact, Eq. (19) is the starting point to interpret FF-SAR imaging as an equivalent, distributed, array. Specifically, $\mathbf{k}(\tilde{\mathbf{P}},\tilde{\mathbf{s}})$ is the wavenumber vector including array wavenumbers corresponding to the reference location $\tilde{\mathbf{P}}$. Consequently, $\Delta\mathbf{P}_{xy}^T\Lambda_s$ is a vector measuring the deviation from these wavenumbers resulting from a ground target displaced by $\Delta\mathbf{P}_{xy}^T$ from $\tilde{\mathbf{P}}$. Hence Λ_s is the sensor transformation matrix [27]-[28] representing the virtual FF-SAR sensor or array, i.e. converting the location of a generic target into the relevant 5-dimension wavenumber vector corresponding to that target.

III. FF-SAR IMAGE SYNTHESIS

According to the array theory basis, the radiation pattern of a generic array is defined as the coherent weighted sum of the signals collected by each element of the array [44]. Suitable weighting functions are adopted to provide the array with some desired features, such as pointing the array towards an assigned direction and filtering out noise or unwanted echoes from specific directions. In the following this approach is applied to the synthetic array defined in Section II. This virtual array includes various elements, represented by the different possible values that the sensor vector $\mathbf{s}$ can take. Those values depend on the available range of frequency, time and baseline components. With specific reference to the available frequency samples, they range from the minimum to the maximum frequency of the transmitted signal, that is $f_m \in [-W/2 ; W/2]$ with $m = 1,\ldots M$, where W is signal bandwidth, M is the total number of frequency samples. The adopted sampling step in frequency, δf, is in inverse relation to the time length of the transmitted pulse. Concerning time, sampled time instants, t_l, $l = 1\ldots L$, belong to the available coherent processing interval sampled at the selected pulse repetition frequency (*PRF*), which can be related to the Doppler bandwidth of the scene. Hence the radiation pattern corresponding to the virtual array derived in Section II can be evaluated as

$$E_{FF-SAR}(\mathbf{P}) = \sum_{i=1}^{N}\sum_{m=1}^{M}\sum_{l=1}^{L} w(\mathbf{s}_{i,m,l})\exp\left(j\Psi(\mathbf{P},\mathbf{s}_{i,m,l})\right) \qquad (20)$$

where w is the selected weighting function. Defining target coordinates with reference to $\tilde{\mathbf{P}}$ and sensor parameters with respect to $\tilde{\mathbf{s}}$, the radiation pattern turns out to be

$$E_{FF-SAR}(\Delta\mathbf{P}_{xy}) =$$
$$\sum_{i=1}^{N}\sum_{m=1}^{M}\sum_{l=1}^{L} w(\Delta\mathbf{s}_{i,m,l})\exp\left(j\left(\mathbf{k}^T\left(\tilde{\mathbf{P}},\tilde{\mathbf{s}}\right)\Delta\mathbf{s}_{i,m,l} + \Delta\mathbf{P}_{xy}^T\Lambda_s\Delta\mathbf{s}_{i,m,l}\right)\right) \qquad (21)$$

As noted above, the applied weighting function depends on the number and the type of conditions that the array pattern must satisfy. The simplest condition one can set is that the peak of the pattern points towards a specific direction, such as the reference location $\tilde{\mathbf{P}}$. This corresponds to

$$w(\Delta\mathbf{s}_{i,m,l}) = \exp\left(-j\left[\mathbf{k}^T\left(\tilde{\mathbf{P}},\tilde{\mathbf{s}}\right)\Delta\mathbf{s}_{i,m,l}\right]\right) \qquad (22)$$

Eqs. (21)-(22) can be interpreted as the generalization of traditional SAR focusing to the case of a distributed SAR. Specifically, they state that the echoes from a specific target, separately collected by each receiver, must be coherently added, that is compensated for the phase difference generated by range frequencies (*m*-index) and azimuth time (*l*-index) but also for phase differences produced when the same target is observed by receivers embarked on different platforms (*i*-index) to get the final focused image of the target. The result is that the derived array pattern plays the same role as the point target response in traditional SAR literature, so it can be used to estimate system performance, such as image resolution, as shown in the next subsections. It is clear that a different determination of weights is required to point the array pattern to any ground target. Again, pointing the array is equivalent to defining the reference function for SAR focusing, e.g. when the reference function varies for different range and azimuth portions in the scene. FF-SAR characterization by the array radiation pattern of Eqs. (21)-(22) implicitly assumes that problems related to focusing can be successfully solved. This includes range walk that, herein, is assumed not to be present or to be compensated for.

The compact notation of Eq. (21) and the introduced quantities w, $\mathbf{k}$, and Λ_s are very useful to characterize the overall FF-SAR imaging performance. Some metrics were introduced in [27] based on Singular Value Decomposition (SVD) of Λ_s and under the assumption that w is a Gaussian function with width and orientation described by the relevant covariance matrix. In the next sections, instead, a different approach is applied making the quantities explicit. This is useful to highlight FF-SAR features, that is the role played by both multiple measurements and spatial diversity.

A. Common and Spatial Diversity Array Patterns

Based on Eq. (22), and without loss of generality, the weighting function is

$$w(\Delta\mathbf{s}_{i,m,l}) = p(\mathbf{B}_i)q(f_m)r(t_l) = p_i\,q_m\,r_l \qquad (23)$$

According to Eqs. (17),(21)-(22) one can write

$$E_{FF-SAR}\left(\Delta\mathbf{P}_{xy}\right) = E_C\left(\Delta\mathbf{P}_{xy}\right)E_{SD}\left(\Delta\mathbf{P}_{xy}\right) \tag{24}$$

with

$$E_C\left(\Delta\mathbf{P}_{xy}\right) = \sum_{m=1}^{M}\left[q_m \exp\left(j\left(2\pi\tau\left(\tilde{\mathbf{P}},\tilde{\mathbf{s}}\right)f_m\right)\right)\right.$$
$$\left.\exp\left(j\left(\Delta\mathbf{P}_{xy}^T 2\pi\nabla_{\mathbf{P}}\tau(\mathbf{P},\tilde{\mathbf{s}})\big|_{\tilde{\mathbf{P}},\tilde{\mathbf{s}}} f_m\right)\right)\right]$$
$$\sum_{l=1}^{L}\left[r_l \exp\left(j\left(2\pi f_D\left(\tilde{\mathbf{P}},\tilde{\mathbf{s}}\right)t_l\right)\right)\right.$$
$$\left.\exp\left(j\left(\Delta\mathbf{P}_{xy}^T 2\pi\nabla_{\mathbf{P}}f_D(\mathbf{P},\tilde{\mathbf{s}})\big|_{\tilde{\mathbf{P}},\tilde{\mathbf{s}}} t_l\right)\right)\right] \tag{25}$$

$$E_{SD}\left(\Delta\mathbf{P}_{xy}\right) = \sum_{i=1}^{N}\left[p_i \exp\left(-j\left(\frac{2\pi}{\lambda}\mathbf{i}_{Rx}^T\left(\tilde{\mathbf{P}},\tilde{\mathbf{s}}\right)\mathbf{B}_i\right)\right)\right.$$
$$\left.\exp\left(-j\left(\Delta\mathbf{P}_{xy}^T\frac{2\pi}{\lambda}\nabla_{\mathbf{P}}\mathbf{i}_{Rx}^T(\mathbf{P},\tilde{\mathbf{s}})\big|_{\tilde{\mathbf{P}},\tilde{\mathbf{s}}}\mathbf{B}_i\right)\right)\right]$$

Hence FF-SAR array pattern is the product of two main contributions:

- The common array pattern E_C, depending on the time delay and the Doppler frequency of the target with respect to the reference receiver. It measures the contribution of a single receiver in the formation as an isolated element.
- The spatial diversity array pattern, E_{SD}, depending on the baselines, i.e. on the spatial separations among the receivers. It characterizes the added value of the FF-SAR in which more receivers are available.

The interpretation of Eq. (25) is as follows. Since all the receivers are relatively close in space ($|\mathbf{B}| << |\mathbf{P}_{Rx}|$), the bistatic SAR images that each receiver generates as an isolated item are very similar. If one considers the amplitudes of their point target response, they are so similar that differences can be neglected in practice. This behavior is modelled by the common array. However, since receivers work from different locations, the phases of the bistatic images are different ($|\mathbf{B}| >> \lambda$) and can be used to synthesize one further array called the spatial diversity array. This is the physical array realized by the relative positions among the receivers in the cluster, properly weighted by beamforming to obtain the desired FF-SAR performance enhancement (see the Section IV). The model of Eqs. (23)-(25) covers a wide range of different SAR schemes. Specifically, FF-SAR can be properly characterized by this model, but even the main properties of simpler realizations, that is more traditional monostatic and bistatic SAR, can be derived. Concerning this, the introduced methodology based on the array theory can easily measure the imaging performance improvement of an FF-SAR with respect to either monostatic or bistatic SARs as it will be pointed out in the remainder of this paper.

Error sources exist affecting FF-SAR imaging: they include synchronization errors and positioning errors. Different forms of synchronization must be applied to enable FF-SAR operations. They can be organized in three main classes [12]: i) spatial synchronization, i.e. receiving antennas are requested to cover the ground area illuminated by the transmitter; ii) echo window or time synchronization. i.e. each receiver must know with sufficient precision the time instants in which echoes from the scene are expected to reach Rx antenna; iii) clock synchronization, i.e. all the receivers must be coherent for the period of time required to get useful data from the scene. A standard assumption is that the transmitter and the receivers are indirectly synchronized at platform level using GPS time, which guarantees an accuracy of 1-2 μs. This is typically enough to support spatial synchronization and, completed by the leap PRF technique [3], guarantees also adequate echo window synchronization. Clock synchronization, instead, is the robust and accurate matching of transmitter and receiver clock phases, with random mean errors smaller than a fraction of a wavelength. Lacking clock synchronization influences both the time (either fast or slow) and the phase of the collected bistatic signals. Clock error is dominated by the frequency offset between the oscillator frequencies of the transmitter and of each receiver. This can be computed accurately using dedicated intersatellite links, as in [4]. An alternative solution for platform with limited resources, e.g. small and micro satellites, or when an illuminator of opportunity is used, is a rough estimation of the offset from the GPS time which is then refined by suitable post-processing of the collected raw bistatic data [45]. As for positioning errors, it is important to remark that tight orbit control is not required for FF-SAR operation [46], which sets instead tight requirements on the knowledge of the relative positions. Specifically, different requirements are posed by bistatic SAR processing and FF-SAR beamforming. The former involves the knowledge of the relative positions between the Tx and each Rx with an accuracy ruled by the ratio between platform velocities and the Doppler bandwidth, i.e. typically below one meter. Beamforming instead requires subwavelength, i.e. up to mm-scale in X-band, accuracy on the knowledge of the baselines among the receivers, which can be achieved by post-processing Carrier-phase Differential GPS (CDGPS) techniques [47]. The following derivations and the simulation results of Section V do not consider error sources. Nonetheless the proposed imaging model based on common and spatial diversity arrays is of quite general validity and simulations could be run to evaluate the effect of either positioning or synchronization errors as outlined in Section VI.

B. Bistatic SAR

If a bistatic SAR is considered, a single receiver is available. In this case no spatial diversity can be exploited

$$E_{SD}\left(\Delta\mathbf{P}_{xy}\right) = 1 \quad \Rightarrow \quad E_{bist}\left(\Delta\mathbf{P}_{xy}\right) = E_C\left(\Delta\mathbf{P}_{xy}\right) \tag{26}$$

with E_{bist} as the representative array pattern of a bistatic SAR,

which can be derived assuming

$$q_m = \exp\left(-j\left(2\pi\tau\left(\tilde{\mathbf{P}},\tilde{\mathbf{s}}\right)f_m\right)\right)$$
$$r_l = \exp\left(-j\left(2\pi f_D\left(\tilde{\mathbf{P}},\tilde{\mathbf{s}}\right)t_l\right)\right)$$

(27)

that is performing bistatic SAR focusing

$$E_{bist}\left(\Delta\mathbf{P}_{xy}\right) =$$
$$\sum_{m=1}^{M}\left[\exp\left(j\left(\Delta\mathbf{P}_{xy}^{T}\,2\pi\nabla_{\mathbf{P}}\tau\left(\mathbf{P},\tilde{\mathbf{s}}\right)\big|_{\tilde{\mathbf{P}},\tilde{\mathbf{s}}}\,f_m\right)\right)\right]$$
$$\sum_{l=1}^{L}\left[\exp\left(j\left(\Delta\mathbf{P}_{xy}^{T}\,2\pi\nabla_{\mathbf{P}}f_D\left(\mathbf{P},\tilde{\mathbf{s}}\right)\big|_{\tilde{\mathbf{P}},\tilde{\mathbf{s}}}\,t_l\right)\right)\right]$$

(28)

The radiation pattern includes two independent contributions given by the inner product between the ground separation $\Delta\mathbf{P}_{xy}$ from the reference position and, respectively, the gradient of the time delay and of the Doppler frequency. This result matches well-known bistatic SAR analyses [34]-[35],[41]-[43],[48]-[50]. A bistatic SAR is able to detect changes of time delay and Doppler frequency and this capability acts along the directions of the gradients of the time delay and of the Doppler frequency, respectively. These directions are, in general, not perpendicular leading to ground pixel skewing. Moreover, the representative array of a bistatic SAR includes time and frequency samples that are regularly spaced and sufficient in number to apply the sinc approximation to the relevant pattern. This means that the point target response is a two-dimensional sinc function with axes aligned to the directions of ground range and Doppler gradients. Corresponding image resolutions can be computed by the so-called gradient method [42]. Nonetheless the same result can be obtained using Eq. (28) and applying the array theory to the derived radiation pattern Indeed, the resolution of an array along a generic direction can be estimated as the projection of the half-power beamwidth of the array along that direction, where, as expected the 3 dB aperture is in direct relation to the wavelength-to-array size ratio [44]. Based on this well-known result, one can formulate ground range and Doppler resolutions as

$$\delta R_g = \chi_f \frac{\lambda}{\Delta R_g} R_b$$
$$\delta a = \chi_t \frac{\lambda}{\Delta a} R_b$$

(29)

where R_b is the bistatic range

$$R_b = \left|\mathbf{P}_{Tx}\left(0\right)-\tilde{\mathbf{P}}\right| + \left|\mathbf{P}_{Rx}\left(0\right)-\tilde{\mathbf{P}}\right|$$

(30)

ΔR_g and Δa are the array sizes along the ground range and Doppler directions, respectively, and χ_f and χ_t are the coefficients of the applied windowing function in frequency and time, e.g. $\chi_f = \chi_t \cong 0.886$ for rectangular windowing. The bistatic radiation pattern of Eq. (28) is used to calculate the array sizes. Namely, the latter are determined considering the total phase angles in Eq. (28) as a function of m and l, respectively, and interpreting those angles as the product of ground range and Doppler wavenumbers with array sizes. Hence,

$$\Delta\Psi_f = k_f\Delta R_g = 2\pi W\left|\nabla_{\mathbf{P},xy}\tau\right|\Delta\mathbf{P}_{xy}^{T}\mathbf{i}_\tau$$
$$\Delta\Psi_t = k_t\Delta a = 2\pi CPI\left|\nabla_{\mathbf{P},xy}f_D\right|\Delta\mathbf{P}_{xy}^{T}\mathbf{i}_{f_D}$$

(31)

where CPI is the coherent processing interval, $\nabla_{\mathbf{P},xy}\tau$ is the ground projection of $\nabla_{\mathbf{P}}\tau\left(\mathbf{P},\tilde{\mathbf{s}}\right)\big|_{\tilde{\mathbf{P}},\tilde{\mathbf{s}}}$, $\mathbf{i}_\tau$ is the unit vector in the direction of $\nabla_{\mathbf{P},xy}\tau$, $\nabla_{\mathbf{P},xy}f_D$ is the ground projection of $\nabla_{\mathbf{P}}f_D\left(\mathbf{P},\tilde{\mathbf{s}}\right)\big|_{\tilde{\mathbf{P}},\tilde{\mathbf{s}}}$, and $\mathbf{i}_{f_D}$ is the unit vector in the direction of $\nabla_{\mathbf{P},xy}f_D$. Based on Eq. (31) one can write

$$k_f = \frac{2\pi}{\lambda}\frac{\Delta\mathbf{P}_{xy}^{T}\mathbf{i}_\tau}{R_b} \qquad \Delta R_g = \lambda R_b W\left|\nabla_{\mathbf{P},xy}\tau\right|$$
$$k_t = \frac{2\pi}{\lambda}\frac{\Delta\mathbf{P}_{xy}^{T}\mathbf{i}_{f_D}}{R_b} \qquad \Delta a = \lambda R_b CPI\left|\nabla_{\mathbf{P},xy}f_D\right|$$

(32)

Hence, bistatic ground range and Doppler resolutions are

$$\delta R_g = \frac{\chi_f}{W\left|\nabla_{\mathbf{P}}\tau\right|}$$
$$\delta a = \frac{\chi_t}{CPI\left|\nabla_{\mathbf{P}}f\right|}$$

(33)

and the amount of pixel skewing is measured as the angle between $\mathbf{i}_\tau$ and $\mathbf{i}_f$, which agrees with equations derived by the gradient method [34],[41],[42].

C. Monostatic SAR

When considering a monostatic SAR, a single receiver exists it is co-located with the transmitter. Therefore, the reference frame of Fig. 1 can be defined with the y-axis parallel to platform velocity and x-z plane as the range elevation plane, such that

$$\mathbf{P}_{Tx}(0) = \mathbf{P}_{Rx}(0) = R \begin{bmatrix} -\sin\theta \\ 0 \\ \cos\theta \end{bmatrix}$$

$$\mathbf{v}_{Tx} = \mathbf{v}_{Rx} = v \begin{bmatrix} 0 \\ 1 \\ 0 \end{bmatrix} \tag{34}$$

$$\mathbf{P} = \begin{bmatrix} 0 \\ 0 \end{bmatrix}$$

where v is platform velocity, R is the slant range of the reference target and θ is the incidence angle. Based on Eq. (15) one derives

$$\nabla_{\mathbf{P},xy}\tau = \frac{2}{c}\begin{bmatrix} -\sin\theta \\ 0 \end{bmatrix} \qquad \mathbf{i}_\tau = \begin{bmatrix} -1 \\ 0 \end{bmatrix} \tag{35}$$

$$\nabla_{\mathbf{P},xy}f_D = \frac{2}{\lambda R}\begin{bmatrix} 0 \\ v \end{bmatrix} \qquad \mathbf{i}_{f_D} = \begin{bmatrix} 0 \\ 1 \end{bmatrix} \tag{36}$$

Using Eqs. (34)-(36) the resulting array size along ground range and azimuth directions are

$$\Delta R_g = \frac{4\lambda RW}{c}\sin\theta$$

$$\Delta a = 4vCPI \tag{37}$$

Replacing Eq. (37) in Eq. (29), the well-known formulas of monostatic SAR resolutions are obtained.

IV. BEAMFORMING OF FF-SAR DATA

According to Section III-A, the spatial diversity array is peaked around the reference location $\tilde{\mathbf{P}}$ as an effect of the introduced weighting functions. The representative radiation pattern of an FF-SAR is thus the result of the spatial diversity array weighting the common array. Since the latter models the image of a generic, isolated, either bistatic or monostatic, receiver of the formation, Eqs. (23)-(25) also represent an example of beamforming applied to the spatial diversity array to provide the FF-SAR with additional properties with respect to the single receiver case.

A. Coherent Resolution Enhancement

Coherent resolution enhancement is achieved by FF-SAR when beamforming is applied as in Eqs. (23)-(25) and the peak of the spatial diversity array is significantly narrower than the main lobe of the common array. As expected, this sets constraints on the size of the spatial diversity array and so on the baseline among the receivers.

As an example, an FF-SAR can be considered including a monostatic side-looking SAR as both the transmitter and the reference receiver of the formation. Depending on the available baselines among the receivers, the spatial diversity array can be

wider than the common, i.e. the monostatic, one thus significantly contributing to the overall FF-SAR array size and to its resolution. Eq. (29) can be still used to quantity the achievable resolution in this case, but differently from the Sections III-B and III-C, $E_{SD}(\Delta\mathbf{P}_{xy}) \neq 1$. The spatial diversity array is defined by the spatial gradient of the unit vector from the reference location to the reference receiver. Based on Eq. (16) and Eq. (34), one derives

$$\nabla_{\mathbf{P}}\mathbf{i}_{Rx}^T(\mathbf{P},\tilde{\mathbf{s}})\big|_{\tilde{\mathbf{P}},\tilde{\mathbf{s}}} = \begin{bmatrix} -\dfrac{\cos^2\theta}{R} & 0 & -\dfrac{\sin\theta\cos\theta}{R} \\ 0 & -\dfrac{1}{R} & 0 \end{bmatrix} \tag{38}$$

where the same reference frame as in Section III-C is used. The resulting FF-SAR array size along ground range and azimuth directions are

$$\Delta R_{g,FF-SAR} = \frac{4\lambda RW}{c}\sin\theta + \Delta B_\perp \cos\theta$$

$$\Delta a_{FF-SAR} = 4vCPI + \Delta B_y \tag{39}$$

where $\Delta B_\perp$ is the maximum baseline component normal to the line-of-sight and ΔB_y is the maximum along-track baseline component. According to Eq. (29), FF-SAR ground range resolution can be computed as

$$\begin{aligned} \delta R_{g,FF-SAR} &= \chi_f \frac{2\lambda R}{\dfrac{4\lambda RW}{c}\sin\theta + \Delta B_\perp \cos\theta} \\ &= \chi_f \frac{c}{2(W+\Delta W)\sin\theta} \end{aligned} \tag{40}$$

with

$$\Delta W = \frac{c\Delta B_\perp}{2\lambda R\tan\theta} \tag{41}$$

where Eqs. (40)-(41) represent standard models used to estimate coherent enhancement of ground range resolution [51]-[53]. Similarly, FF-SAR azimuth resolution is

$$\delta a_{FF-SAR} = \chi_t \frac{2\lambda R}{4vCPI + \Delta B_y} = \frac{\delta a_{mono}}{1+\dfrac{\Delta B_y}{2vCPI}} \tag{42}$$

where δa_{mono} is the monostatic SAR azimuth resolution and the ratio $\Delta B_y/(2vCPI)$ corresponds to the non-overlapping fraction of interferometric area, introduced in [54] to quantify the coherent azimuth resolution enhancement of an interferometric cartwheel. Hence, the derivation confirmed that Eq. (29)

reduces to standard models [51]-[54] of coherent resolution enhancements when a monostatic SAR, working in side-looking geometry, is used as both the illuminator and the reference receiver of an FF-SAR.

As a further confirmation of the versatility of array theory for the interpretation of FF-SAR imaging properties, even the concept of critical baselines [12] can be retrieved. Indeed, it is well-known that coherent resolution enhancement is limited by the condition that receivers are separated by a distance that is shorter than the critical value. In the same way, within array theory, baselines among FF-SAR receivers are much longer than signal wavelength. So, the spatial diversity array is, by definition, a sparse array [40],[44] and strong grating lobes as the peak towards the reference position appear. Those grating lobes are not a problem as long as the overall FF-SAR array is not sparse. More precisely, conditions exist in which grating lobes of the spatial diversity array are strongly attenuated by the common array. For very long baselines and very dispersed receivers, that is when one tries to drastically improve resolution by using a limited number of receivers, several grating lobes can appear in the FF-SAR array pattern. As a rule of thumb, satisfactory performance is always achieved if no grating lobe of the spatial diversity pattern occurs within the main lobe of the common array. To quantify this rule, it is worth considering monostatic side-looking SAR augmented by a single receiver forming only a horizontal baseline component ΔB_x. The spatial diversity array in this case corresponds to that of a dipole antenna [40] and it is characterized by grating lobes at angles $\theta_{G,k}$, where

$$\sin \theta_{G,k} = \sin \theta \pm k \frac{\lambda}{\Delta B_x} \qquad (43)$$

with k integer number. As noted above, to ensure good FF-SAR performance it is desired that grating lobes fall outside the main lobe of the monostatic point target response in ground range. If $\Delta \theta_{NTN}$ is the null-to-null width corresponding to the monostatic point target response, that is

$$\Delta \theta_{NTN} = 2 \frac{\delta R_g \cos \theta}{R} \qquad (44)$$

the condition to satisfy is

$$\theta_{G,1} \geq \theta + \frac{\Delta \theta_{NTN}}{2} \qquad (45)$$

Since one can write

$$\theta_{G,1} = \theta + \Delta \theta_G \qquad \Delta \theta_G \ll 1 \qquad (46)$$

substituting Eq. (46) in Eq. (43) and then in Eq. (45) yields

$$\Delta B_\perp \leq \frac{\lambda R}{\delta R_g \cos \theta} \qquad (47)$$

The right term in Eq. (47) is the so-called critical orthogonal baseline [12]. Hence requiring the spatial diversity array to show grating lobes outside the main lobe of the monostatic point target response means setting the orthogonal baseline shorter than the critical value. Moreover, it is worth noting that Eq. (47) corresponds to $\Delta W \leq W$ in Eq. (41), that is the ground range resolution improvement is limited to a factor of 2. The result can be extended to the case of an FF-SAR working with more receivers. Grating lobes for an array of N uniformly displaced elements occur at angles that are still ruled by Eq. (43) if ΔB_x is interpreted as the distance between adjacent elements. Therefore, if the latter is shorter than the critical value, no grating lobes of the spatial diversity array fall into the main lobe of the monostatic response. This result seems to suggest that by using a formation of N uniformly displaced receivers one can enhance the ground range resolution by a factor of N. However, care must be taken in combining data collected from baselines close to the critical value, which are, no doubt, subject to baseline decorrelation effects. The same approach can be applied to the azimuth direction leading to the same conditions as in [54] for coherent resolution enhancement in azimuth.

One further case to consider is an FF-SAR working with N receivers that are not regularly displaced. In this case, as long as separations show no periodicity [40],[44], no real grating lobes (i.e. as strong as the main lobe) appear, although high spurious lobes may be present, which occur outside the main lobe of the monostatic response.

The above derivation can be further generalized to the case in which an FF-SAR is used, exploiting a transmitter working on an independent trajectory, i.e. an illuminator of opportunity. In this case the common array corresponds to the bistatic array of the reference satellite. So, Eq. (29) is still valid to represent FF-SAR image resolution if the total array size is considered along both range and Doppler directions. According to Eq. (25), FF-SAR total phase angles along $\mathbf{i}_\tau$ and $\mathbf{i}_f$ are, respectively,

$$\Delta \Psi_{f,FF-SAR} =$$
$$\frac{2\pi}{\lambda} \frac{\Delta \mathbf{P}_{xy}^T \mathbf{i}_\tau}{R_b} \left(\lambda R_b W \left| \nabla_{\mathbf{P},xy} \tau \right| + R_b \mathbf{i}_\tau^T \left. \nabla_{\mathbf{P}} \mathbf{i}_{Rx}^T (\mathbf{P},\tilde{\mathbf{s}}) \right|_{\tilde{\mathbf{P}},\tilde{\mathbf{s}}} \Delta \mathbf{B} \right)$$
$$= k_f \Delta R_{g,FF-SAR}$$

$$\Delta \Psi_{t,FF-SAR} =$$
$$\frac{2\pi}{\lambda} \frac{\Delta \mathbf{P}_{xy}^T \mathbf{i}_{fD}}{R_b} \left(\lambda R_b CPI \left| \nabla_{\mathbf{P},xy} f_D \right| + R_b \mathbf{i}_{fD}^T \left. \nabla_{\mathbf{P}} \mathbf{i}_{Rx}^T (\mathbf{P},\tilde{\mathbf{s}}) \right|_{\tilde{\mathbf{P}},\tilde{\mathbf{s}}} \Delta \mathbf{B} \right)$$
$$= k_t \Delta a_{FF-SAR}$$
$$(48)$$

where $\Delta \mathbf{B}$ is the vector of the maximum baseline components. Hence, FF-SAR resolutions become

$$\delta R_{g,FF-SAR} = \chi_f \frac{1}{W\left|\nabla_{\mathbf{P},xy}\tau\right| + \frac{1}{\lambda}\mathbf{i}_\tau^T \nabla_{\mathbf{P}}\mathbf{i}_{Rx}^T\left(\mathbf{P},\tilde{\mathbf{s}}\right)\Big|_{\tilde{\mathbf{P}},\tilde{\mathbf{s}}} \Delta\mathbf{B}}$$

$$\delta a_{FF-SAR} = \chi_t \frac{1}{CPI\left|\nabla_{\mathbf{P},xy}f_D\right| + \frac{1}{\lambda}\mathbf{i}_{f_D}^T \nabla_{\mathbf{P}}\mathbf{i}_{Rx}^T\left(\mathbf{P},\tilde{\mathbf{s}}\right)\Big|_{\tilde{\mathbf{P}},\tilde{\mathbf{s}}} \Delta\mathbf{B}} \qquad (49)$$

It is worth noting that, Eqs. (40),(42),(49) represent an approximate estimate of FF-SAR resolution. This is because they implicitly assume the spatial diversity array to include regularly spaced elements, in a number sufficient to model peak sections along ground range and Doppler directions as sinc functions. When the number of adopted receivers is low, and receivers are irregularly displaced, the resulting spatial diversity pattern can notably deviate from a sinc-like shape. In this case a viable solution for estimating FF-SAR resolution is the numerical simulation of the radiation patterns (see Section V).

Concluding this section on coherent resolution enhancement it is important to clarify that both the common and the spatial diversity arrays are representative of FF-SAR performance when the effect of perturbing phenomena like topography is negligible or it can be compensated for [12],[52].

B. SNR Improvement

Interpreting coherent resolution enhancement as just the improvement of nominal resolutions of the reference bistatic SAR means limiting FF-SAR capabilities. Indeed, not only δR_g and δa can be improved, but bistatic response can be drastically modified. As an example, pixel skewing achieved in either squinted monostatic or bistatic SAR geometries can be attenuated. Moreover, even when the sizes of the spatial diversity array are small, thus not allowing for resolution enhancement, additional features can be achieved. This is the case of coherent Signal-to-Noise Ratio (SNR) improvement and High-Resolution Wide-Swath (HRWS) Imaging. The latter is fully analyzed in Section IV-C whereas the former is briefly presented herein. Specifically, working with N receivers, as an effect of the coherent combination of Eq. (24), the SNR achieved by an FF-SAR is the sum of the SNR of each bistatic receiver. Moreover, if the spatial diversity array is small, so that short baselines are established, no resolution enhancement is achieved, but range variations among the receivers can be neglected, thus making it possible to assume that the SNR is the same for all receivers. So, SNR can be improved up to a factor given by the number of adopted receivers. Finally, for those, short baseline, formations, even though the spatial diversity array is still sparse, the relevant grating lobes are not a matter of concern for the FF-SAR, since they are strongly attenuated by the common array.

C. Null-steering and HRWS imaging

Null-steering can be applied to the spatial diversity array for providing FF-SAR array pattern with additional features. Indeed, even when the condition of Eq. (22) is set, that is both common and spatial diversity array patterns are steered towards a specific

target, further degrees of freedom are available. This is evident from the definition of $E_{SD}\left(\Delta\mathbf{P}_{xy}\right)$ in Eq. (25). Specifically, this represents a single scalar condition affecting the N available $p_i\left(\mathbf{B}_i\right)$ weights. Hence, the weights of the spatial diversity array are still able to satisfy an additional N-1 conditions, i.e. a more general beamforming problem can be formulated for the spatial diversity array including both beam and null-steering. Following Eq. (25), a steering function can be defined

$$\phi\left(\mathbf{B}_i, \Delta\mathbf{P}_{xy}\right) =$$
$$\exp\left[-j\left(\frac{2\pi}{\lambda}\mathbf{i}_{Rx}^T\left(\tilde{\mathbf{P}},\tilde{\mathbf{s}}\right)\mathbf{B}_i + \frac{2\pi}{\lambda}\Delta\mathbf{P}_{xy}^T\nabla_{\mathbf{P}}\mathbf{i}_{Rx}^T\left(\mathbf{P},\tilde{\mathbf{s}}\right)\Big|_{\tilde{\mathbf{P}},\tilde{\mathbf{s}}}\mathbf{B}_i\right)\right] \qquad (50)$$

and adding null-steering constraints to the spatial diversity array leads to the following problem

$$\begin{cases} p\left(\mathbf{B}_i\right)\phi\left(\mathbf{B}_i, 0\right) = 1 \\ p\left(\mathbf{B}_i\right)\phi\left(\mathbf{B}_i, \Delta\mathbf{P}_{null,g}\right) = 0 \end{cases} \quad i = 1,...,N \quad g = 1,...,G-1 \qquad (51)$$

where $\Delta\mathbf{P}_{null,g}$ is the gth ground location toward which a null of the spatial diversity array must be set. The problem of Eq. (51) can be recast in a standard linear form

$$A\mathbf{p}_{SD} = \mathbf{e}_1 \qquad (52)$$

where $\mathbf{p}_{SD}$ is the unknown vector

$$\mathbf{p}_{SD} \in \mathbb{R}^{Nx1} \Rightarrow \mathbf{p}_{SD} = \begin{bmatrix} p\left(\mathbf{B}_1\right) & \cdots & p\left(\mathbf{B}_N\right) \end{bmatrix}^T \qquad (53)$$

A is the steering matrix

$$A \in \mathbb{R}^{GxN} \Rightarrow A = \begin{bmatrix} \boldsymbol{\phi}^T\left(0\right) \\ \boldsymbol{\phi}^T\left(\Delta\mathbf{P}_{null,1}\right) \\ \vdots \\ \boldsymbol{\phi}^T\left(\Delta\mathbf{P}_{null,G-1}\right) \end{bmatrix} \qquad (54)$$

with

$$\boldsymbol{\phi}\left(\Delta\mathbf{P}_{null}\right) \in \mathbb{R}^{Nx1} \Rightarrow$$
$$\boldsymbol{\phi}\left(\Delta\mathbf{P}_{null}\right) = \begin{bmatrix} \phi\left(\mathbf{B}_1, \Delta\mathbf{P}_{null}\right) & \cdots & \phi\left(\mathbf{B}_N, \Delta\mathbf{P}_{null}\right) \end{bmatrix}^T \qquad (55)$$

and

$$\mathbf{e}_1 \in \mathbb{R}^{G\times1} \Rightarrow \mathbf{e}_1 = \begin{bmatrix} 1 & 0 & \cdots & 0 \end{bmatrix}^T \qquad (56)$$

If $G \leq N$, it is well-known that one solution of Eq. (52) is

TABLE I
SIMULATION PARAMETERS FOR SENTINEL 1D AND STEREOID MONOSTATIC-BISTATIC SYSTEM [30].

Parameter	Value
Wavelength	0.055 m
Satellite Altitude	693 km
Tx Signal Bandwidth	80 MHz
Incidence Angle	33.7°
Tx Antenna Size	12.3 m x 0.82 m
Tx Pulse Length	30 μs
Monostatic CPI	0.42 s
PRF	1.49 kHz
Rx Antenna Size	1.3 m x 0.8 m
Rx Along-track Baseline	345 km
Bistatic CPI	0.56 s
Tx Position	[-452 km, -0.03 km, 678 km]
Tx Velocity	[0 km/s, 7.59 km/s, 0 km/s]
Rx Position	[-451 km, -344 km, 670 km]
Rx Velocity	[-0.02 km/s, 7.58 km/s, 0.4 km/s]

$$\mathbf{w}_{SD} = A^H \left(AA^H \right)^{-1} \mathbf{e}_1 \qquad (57)$$

where $A^H \left(AA^H \right)^{-1}$ is the pseudo-inverse matrix of A.

Based on the introduced beamforming problem, HRWS imaging can be formulated as an application of FF-SAR, which aims at overcoming the close relationship existing between the azimuth resolution and the width of the unambiguous swath [9]. For either a monostatic or a bistatic SAR, high resolution in the Doppler direction requires a wide Doppler bandwidth, which, in turn, implies a high PRF for proper sampling. On the other hand, high operating PRF values lead to strong limitations on the unambiguous swath intervals in range, due to range ambiguities. Hence, a high azimuth resolution implies a small unambiguous swath width and vice versa. An FF-SAR system is able to break this inverse relationship by jointly exploiting samples gathered by several platforms [25]-[26]. In this concern, the array theory is, again, a very powerful tool to represent FF-SAR application to HRWS. Namely, if the PRF required to achieve an assigned large swath width is too low, proper sampling of the Doppler bandwidth cannot be performed. Consequently, the common array $E_C \left(\Delta \mathbf{P}_{xy} \right)$ shows grating lobes which are referred to as azimuth, or Doppler, ambiguities [9],[55]. Those gratings are placed in locations $\mathbf{P}_A$ corresponding to Doppler frequencies that are offset by integer multiples of the PRF from the Doppler frequency of $\tilde{\mathbf{P}}$. According to Eq. (10)

$$-\frac{1}{\lambda} \mathbf{v}_{Tx}^T \frac{\left(\mathbf{P}_{Tx}(0) - \mathbf{P}_{A,d} \right)}{\left| \mathbf{P}_{Tx}(0) - \mathbf{P}_{A,d} \right|} - \frac{1}{\lambda} \mathbf{v}_{Rx}^T \frac{\left(\mathbf{P}_{Rx}(0) - \mathbf{P}_{A,d} \right)}{\left| \mathbf{P}_{Rx}(0) - \mathbf{P}_{A,d} \right|} \qquad (58)$$
$$= f_D \left(\tilde{\mathbf{P}}, \tilde{\mathbf{s}} \right) + d\,PRF \qquad d = \pm 1, \pm 2, ..$$

Nonetheless, if null-steering of the spatial diversity array is applied, with nulls corresponding to the locations of the

ambiguities, grating lobes of the common array are suppressed in the resulting FF-SAR array pattern.

V. SIMULATION RESULTS

The concepts of radiation pattern and array synthesis are first applied to a monostatic-bistatic SAR configuration. This is the case of STEREOID mission [30] conceived as a companion satellite augmenting Sentinel-1D capability. The space segment of the mission consists of two identical sub-500 kg class spacecraft carrying a receive-only radar instrument as the main payload and flying in a re-configurable formation with Sentinel-1D. Both monostatic and bistatic images are thus available for the observed areas. The augmentation is based on the use of several azimuth lines-of-sight to support precise measurements of small-scale motion and deformation fields of the ocean surface, glaciers and ice sheets, and solid Earth. Table I lists the main parameters of Sentinel-1D that are used for the simulation of the monostatic radiation pattern.

For the sake of simplicity, computation is performed introducing a reference frame with origin in the simulated point target, z-axis as the local vertical direction, (x,y) as the local ground plane, with y-axis along Sentinel-1D platform velocity. The simulated radiation pattern is depicted in Fig. 2. The expected behavior of the point target response of a monostatic SAR is correctly reconstructed (Fig. 2a) as a 2D sinc function with orthogonal axis aligned with ground range and azimuth directions according to monostatic iso-range and iso-Doppler lines (Fig. 2b). The analysis of ground range and azimuth cuts (Fig. 2c and Fig. 2d) of the radiation pattern confirms that the introduced method models the point target response in a proper way leading to 3.0 m ground range and 6.2 m azimuth resolution, respectively. Performance parameters like PSLR and ISLR are also in line with image focusing by rectangular weighting functions.

Bistatic SAR imaging performance can be also analyzed by the relevant radiation pattern. Fig. 3 shows the results considering one bistatic receiver of STEREOID placed along the same orbit of Sentinel-1D with a mean anomaly difference realizing an along-track separation of more than 340 km (see Table I). As expected, the 2D radiation pattern (Fig. 3a) is still a 2D sinc function but the relevant axes are no longer orthogonal, being characterized by a skew angle of about 105° which is confirmed by the analysis of iso-range and iso-Doppler curves (Fig. 3b). Cuts of the 2D radiation pattern are also analyzed along both iso-Doppler (Fig. 3c) and iso-range (Fig. 3d) lines, where the natural sinc-like shape can be recognized. The estimated point target response widths are, respectively, 2.9 m along the iso-Doppler line and 5.2 m along the iso-range one. The results agree with Eq. (33) and with the gradient method. In detail, the latter computes the distance between two iso-range (iso-Doppler) curves separated by a time delay (Doppler frequency) of χ_f / W (χ_t / CPI). This distance is shorter than the distance between the same iso-range (iso-Doppler) lines computed along the iso-Doppler (iso-range) curve by a factor depending on the skew angle as shown in Fig. 4. So, one can retrieve the above reported
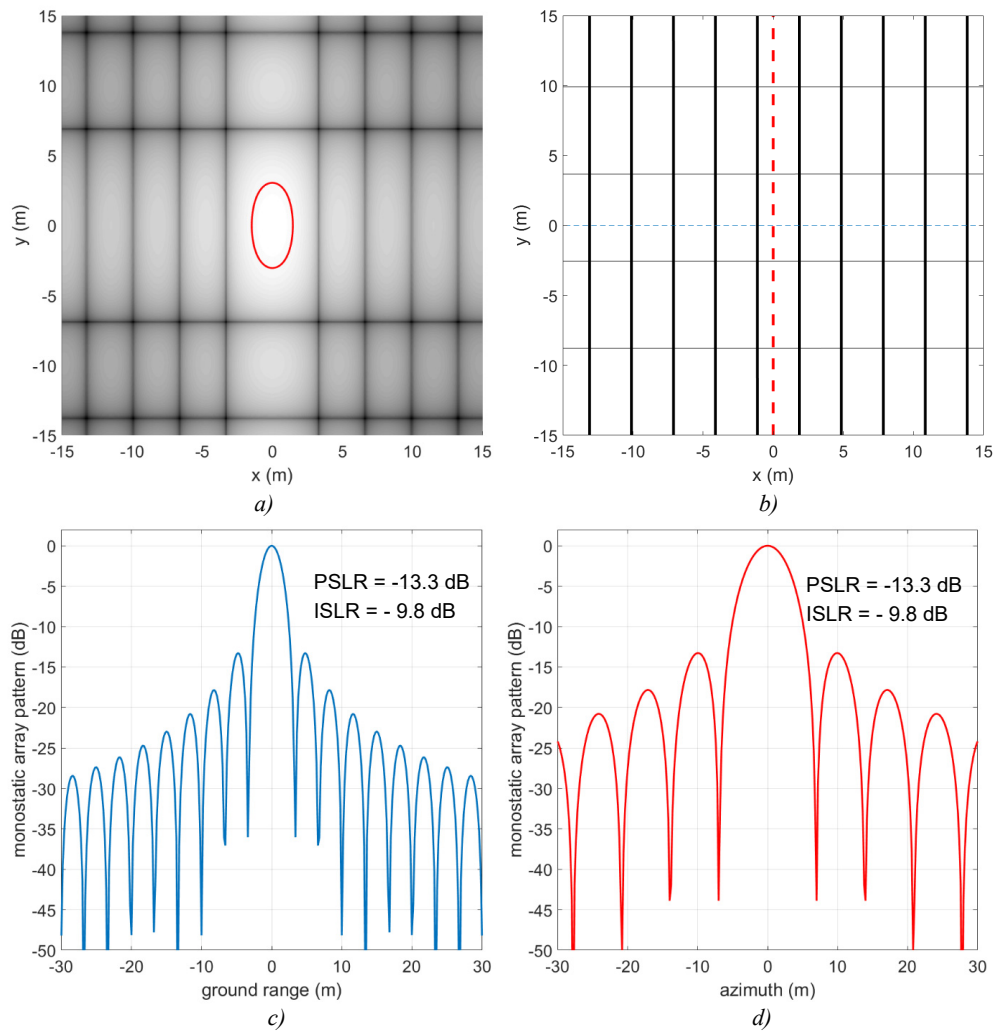
Fig. 2. Simulated monostatic SAR radiation pattern for Sentinel-1D: *a)* point target response; *b)* iso-range (thick) and iso-Doppler (thin) curves; *c)* ground range cut of the 2D radiation pattern along the thin dotted line of *b)*; *d)* azimuth cut of the 2D radiation pattern along the thick dotted line depicted of *b)* . Bold line in *a)* indicates the -3dB curve.

values of 2.9 m and 5.2 m by Eq. (33) and then multiplying the estimated ground range and Doppler resolution by the sine of the skew angle.

As an example of a multi-static FF-SAR mission, a satellite formation including 6 microsatellites is simulated. One platform is a Tx/Rx one whereas the other 5 satellites are Rx-only. The system has been preliminarily designed to operate from an altitude of 500 km and to guarantee -25dB noise equivalent sigma zero (NESZ) within a swath width of 30 km by just 1 kW peak power and 2 m^2 antenna area. The main system parameters are listed in Table II.

The formation is characterized by a dominant along-track baseline component but residual vertical and cross-track baselines are present, which are used to partially decouple the collision risk from the along-track design [56]. The working principle is based on the application of beamforming on the signal collected by the six receivers to obtain HRWS imaging and to exploit the residual redundancy to work with low Tx power. Indeed, the assigned antenna area and swath width set timing

requirements that cannot be easily fulfilled by a single-platform, single-channel, system. Nominal operations of an FF-SAR system implementing the principle of HRWS imaging involves data collection from receivers working with pure along-track separations without any orthogonal baseline component. Such an assumption can be made for HRWS systems operating from a single-platform using multi-channel antennas as receivers, e.g. [31], but it is unrealistic for an FF-SAR. Cross-track and vertical baseline components generate additional phase contributions depending on surface topography too. Therefore, beamforming to be applied on the received signals must include a correction accounting for the topographic phase [23].

Fig. 5a shows the simulated common radiation pattern, i.e. the radiation pattern representing the point target response of the Tx/Rx satellite, along an iso-range line. Since the Doppler bandwidth is under-sampled, azimuth ambiguities arise. Nonetheless, according to Section IV-C the spatial diversity array pattern can be adjusted to perform null-steering and to suppress the ambiguities in the resulting FF-SAR radiation pattern. Fig. 5b
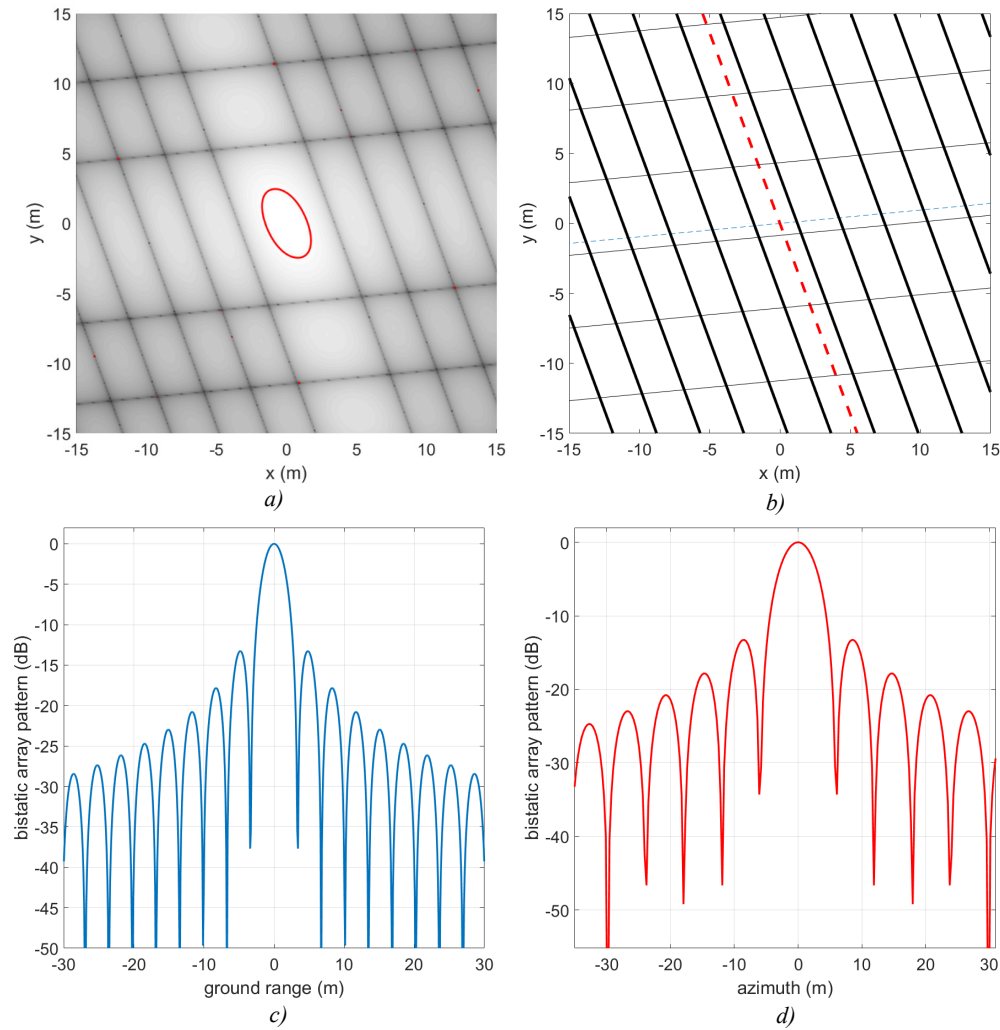
Fig. 3. Simulated bistatic SAR radiation pattern for one receiver of STEREOID mission with large along-track baseline: *a)* point target response; *b)* iso-range (thick) and iso-Doppler (thin) curves; *c)* ground range cut of the 2D radiation pattern along the thin dotted line of *b)*; *d)* azimuth cut of the 2D radiation pattern along the thick dotted line depicted of *b)* . Bold line in *a)* indicates the -3dB curve.
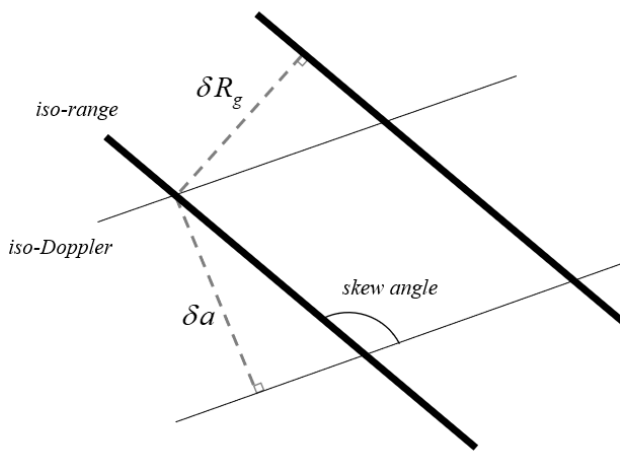

Fig. 4. Illustration of the skewing effect in bistatic SAR imaging

TABLE II
SIMULATION PARAMETERS FOR HRWS THROUGH A FORMATION OF MICROSATELLITES.

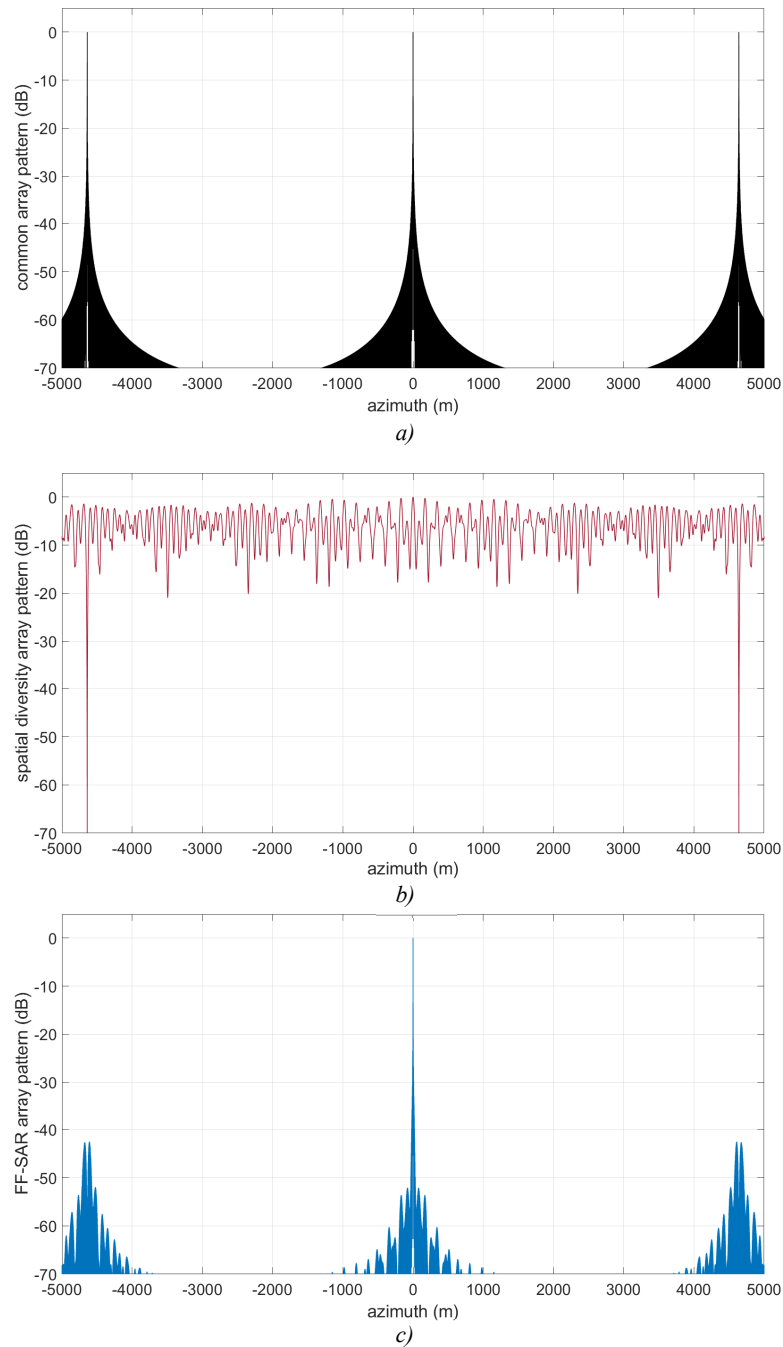| Parameter	Value
Wavelength	0.031 m
Satellite Altitude	500 km
Incidence Angle	25.5°
Tx Antenna Size	2 m x 1 m
CPI	0.98 s
PRF	4.139 kHz
Rx Antenna Size	2 m x 1 m
Tx Position	[-25 km, -0.01 km, 495 km]
Tx Velocity	[0 km/s, 7.69 km/s, 0 km/s]
Number of Receivers	6
Along-track Baselines	[-313 m, -209 m, -103 m, 0 m, 92 m, 193 m]
Vertical Baselines	[35 m, 24 m, 17 m, 0 m, -18 m, -40 m]
Cross-track Baselines	[21 m, -2 m, 22 m, 0 m, -3 m, 44 m]

Fig. 5. Simulated radiation pattern for a formation of microsatellites: *a)* common radiation pattern; *b)* spatial diversity radiation pattern; *c)* FF-SAR point target response. System parameters listed in Table II.

depicts the spatial diversity array obtained by the steering function and the null-steering conditions of Eq. (51) and Eq. (58). The resulting FF-SAR array pattern is shown in Fig. 5c. Efficient suppression of azimuth ambiguities is obtained. With reference to Fig. 5b, it is worth nothing that the spatial diversity array is affected by strong grating lobes. However, as discussed in Section IV-C, those grating lobes fall outside the main beam of the common radiation pattern (see Fig. 6). Hence their effect on the quality of the resulting FF-SAR image is negligible.

The above presented example dealt with a multistatic system in which FF-SAR is used to improve the performance of a monostatic, single-channel, SAR in terms of swath width and SNR. Nominal resolutions of the Tx/Rx monostatic satellite are unaltered (Fig. 6). However, FF-SAR features can be exploited to realize a multistatic system able to bypass bistatic SAR imaging limitations, e.g. coarse resolution and pixel skewing, but also, depending on system parameters, narrow unambiguous swath. Array theory, once again, is a valuable tool for assessing FF-SAR capabilities in this ambit.

TABLE III
SIMULATION PARAMETERS FOR AN FF-SAR BASED ON DVB-T SIGNAL
TRANSMISSION (TX SIGNAL PARAMETERS ADAPTED FROM [57]).

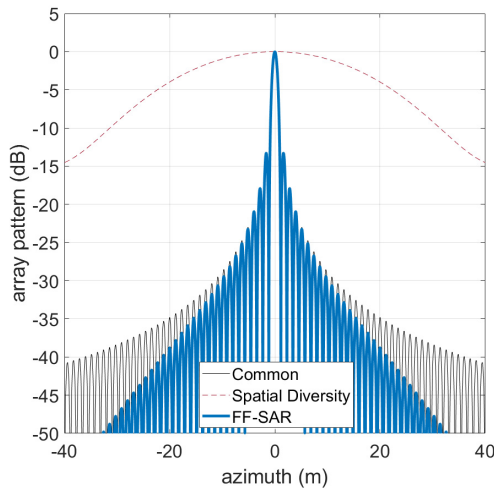| Parameter	Value
Wavelength	0.46 m
Tx Signal Bandwidth	7.7 MHz
Symbol Length	896 μs
Tx Position	[-7.78 km, -7.78 km, 0.23 km]
Rx Position	[0,0,400 km]
Rx Velocity	[0 km/s,7.67 km/s,0 km/s]
Rx Antenna Aperture	5°
CPI	4.54 s
Number of Receivers	7
Along-track Baselines	[-300 m, -200 m, -100 m, 0 m, 100 m, 200 m, 300 m]
Cross-track Baselines	[-5700 m -5130 m, -3420 m, 0, 1140 m 2850 m, 3990 m]

Fig. 6. Zoomed view, around target location, of the radiation pattern for a formation of microsatellites.

Another case considered is the PASSAT (Passive SAR satellite constellation) concept [56], in which transmitters of opportunity are ground-based broadcasting stations, in form of DVB-T signals and receivers are onboard Low Earth Orbit (LEO) satellites. Receivers are assumed to be arranged into a satellite constellation to achieve the desired temporal and spatial coverage.

The imaging performance of the bistatic system including a single DVB-T station and a single LEO receiver is analyzed in [56]. Indeed, DVB-T signals show a complex structure able to transmit compressed digital audio, video, and other data using Coded Orthogonal Frequency Division Multiplexing (COFDM): data are delivered in a series of discrete blocks or symbols at the so-called symbol rate. Nonetheless suitable processing can be applied [56] allowing one to interpret single symbols as radar pulses characterized by about 8 MHz bandwidth. Symbol duration, useful for radar imaging is about 896 μs which leads to a maximum equivalent PRF of about 1.1 kHz. As an example of bistatic geometry for PASSAT, a generic DVB-T broadcasting station is assumed as a 230 m high tower illuminating a target which is about 11 km distant. A nadir looking satellite receiver is

also simulated orbiting at about 400 km altitude. Further system parameters are listed in Table III. Fig. 7a and Fig. 7b show, respectively, the bistatic array radiation pattern and iso-range and iso-Doppler lines. The origin of the reference frame is target location and receiver velocity is along the y-axis, with, again, (x,y) as the ground plane. According to the gradient method the resolution along the x-axis is 48.8 m, whereas the resolution along y-axis is 4.7 m, and a significant skew angle of 135° arises. Those values agree with the simulated array radiation pattern of Fig. 7a. Furthermore, owing to the limited equivalent PRF, azimuth under-sampling occurs. The Doppler bandwidth is about 1.45 Hz, so azimuth or Doppler ambiguities dominate the radiation pattern (see Fig. 7c).

Imaging performance is notably improved when each receiver of PASSAT constellation is replaced by an FF-SAR. In detail, provided that a sufficient number of properly separated formation flying receivers can be deployed, the resolution along the x-axis can be enhanced and the first azimuth ambiguities can be suppressed. According to Table III, a formation of 7 satellites is simulated, characterized by a dominant separation along the x-axis and residual baseline components along y-axis. Based on this geometric arrangement, the FF-SAR array radiation pattern can be computed, steering the beam of the spatial diversity array towards target location and forcing nulls in the direction of the first azimuth ambiguities.

Fig. 8 shows the estimated radiation patterns around target location. According to the simulated baseline components the spatial diversity array pattern (Fig. 8b) features a narrow peak along the x-axis but very limited discrimination capabilities along y-axis.

As a result, the realized FF-SAR achieves much better resolution (Fig. 8a) compared to the case of a single bistatic receiver (Fig. 7a). Fig. 8c shows the cut of the radiation pattern along x-axis. FF-SAR point target response width is about 10 m, together with -9 dB PSLR. Concerning the latter value, it is worth nothing that, because of the limited number of receivers, the spatial diversity array pattern is far from showing a sinc-like behavior. Hence the cost to pay for a significant improvement of the point target response width by using several receivers is a degradation of the side-lobe level.

Fig. 9 illustrates the ambiguity rejection capabilities of the simulated FF-SAR. Differently from the former example of short formation (Fig. 5), the capability of null-steering to reduce the ambiguous power is weakened. This is because setting a null in the radiation pattern of a longer array naturally affects a smaller image portion (see Fig. 9d). Nonetheless ambiguities in the FF-SAR image are more than 26 dB lower than the relevant target which can be acceptable for imaging purposes.

VI. CONCLUSION

Imaging properties of monostatic, bistatic, and multistatic SAR can be recast into a single theoretical framework by the array theory. Indeed, when a single receiver is considered, the introduced common array pattern models time delays and Doppler frequencies of the observed targets. Moreover, for a multistatic SAR the effect of the physical separation among the
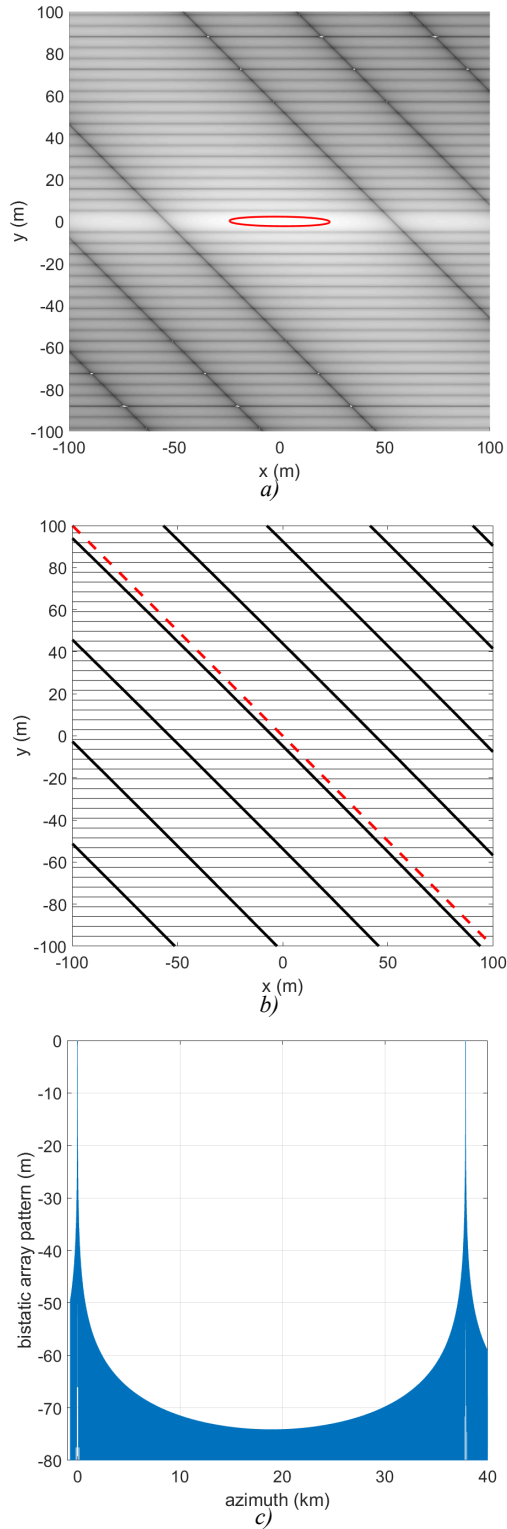
Fig. 7. Simulated radiation pattern for the bistatic system including a ground-based DVB-T tower as the transmitter and a nadir-looking LEO satellite as the receiver: *a)* point target response; *b)* iso-range (thick) and iso-Doppler (thin) curves; *c)* azimuth cut of the 2D radiation pattern along the thick dotted line depicted of *b)* . Bold line in *a)* indicates the -3dB curve. System parameters are listed in Table III.
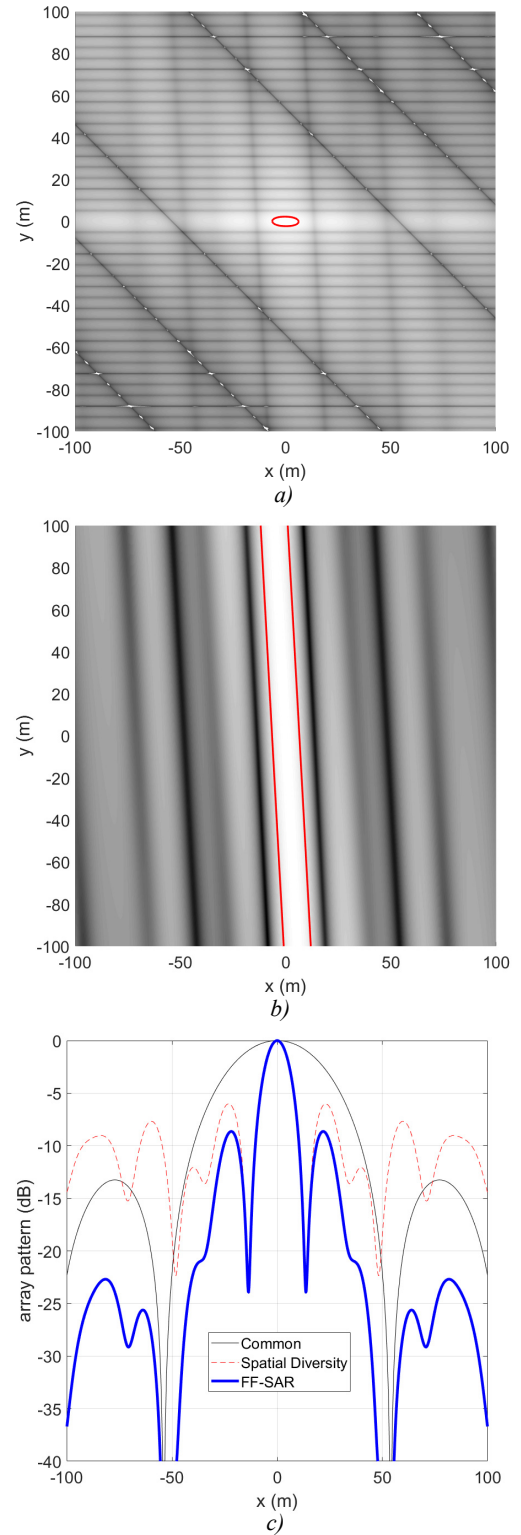
Fig. 8. Simulated radiation pattern for an FF-SAR using a ground-based DVB-T tower as the transmitter: *a)* FF-SAR point target response; *b)* 2D spatial diversity array pattern; *c)* cut of the 2D radiation patterns along x-axis. Bold lines in *a)* and *b)* indicates the -3dB curve. System parameters are listed in Table III.
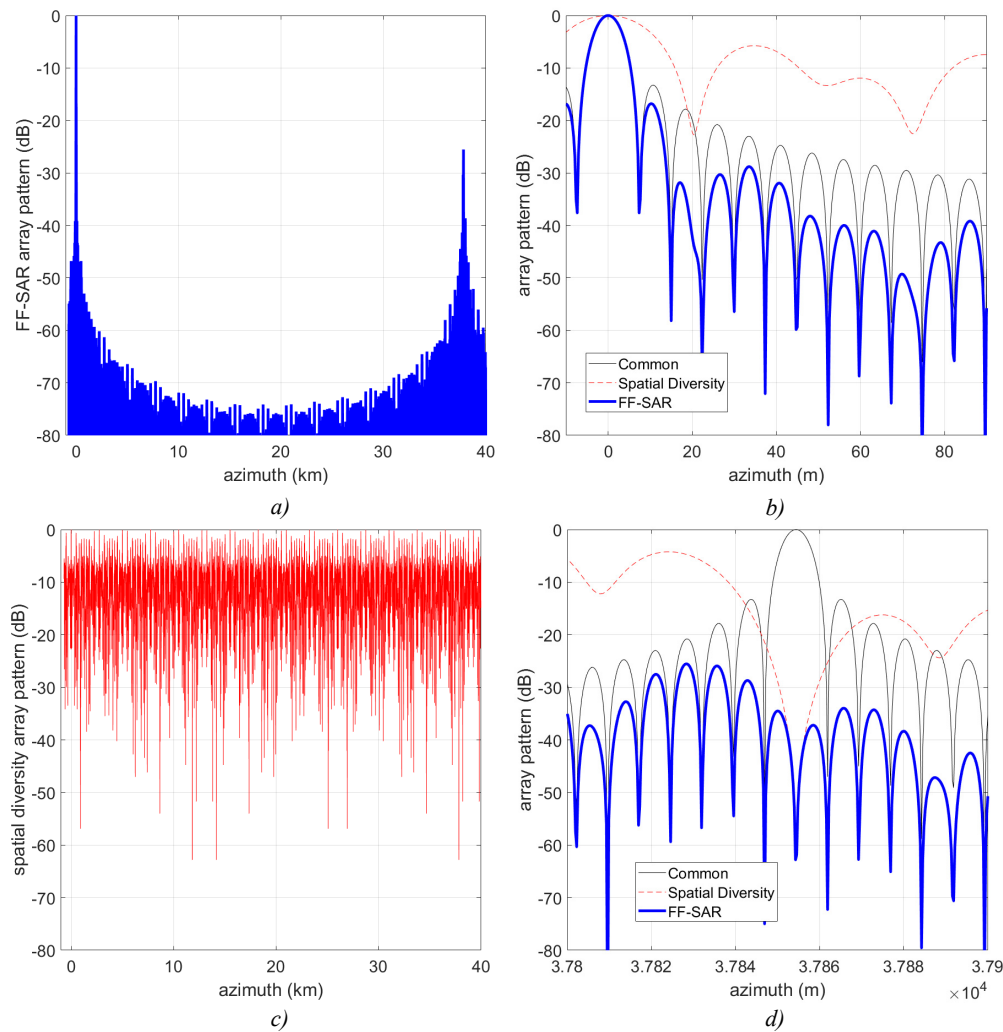
Fig. 9. Azimuth cuts of the simulated radiation pattern for an FF-SAR using a ground-based DVB-T tower as the transmitter: *a)* FF-SAR point target response; *b)* zoomed view around target location; *c)* spatial diversity array radiation pattern; *d)* zoomed view around ambiguity location.

receivers is described by the defined spatial diversity array. This paper focused on a specific realization of a multistatic SAR, referred to as FF-SAR. This is based on a cluster of satellite receivers flying in coordinated motion with separations in both along-track and cross-track/vertical directions. The introduced methodology allows the measurements of the performance improvement of an FF-SAR with respect to more traditional systems like monostatic and bistatic SAR. Both proper selection of baselines among the receivers and beamforming of the spatial diversity array contribute to FF-SAR imaging. However, presented simulations confirmed that, even though the spatial diversity array is, by definition, a sparse array, receiving platforms must not be evenly or regularly spaced, hence tight control of relative positions is not required. Baselines among the receivers can drift. This does not degrade imaging capabilities significantly if suitable solutions for beamforming can be applied. The theoretical and simulation analyses of this paper have some limits depending on the relevant assumptions. Straight path and constant velocities were assumed for both the transmitter and the receivers within the coherent processing

interval. This is a good approximation to characterize imaging performance, but it is inadequate for some bistatic and multistatic focusing steps, like motion compensation, in which the curvature of the orbits must be accounted for. Hence, FF-SAR performance estimated in the present work is valid if suitable solutions are applied for bistatic SAR focusing and beamforming, which are already available in the literature. The proposed signal model was derived considering a flat scene, so, if orthogonal baselines are involved, the model can be applied when topography can be neglected or reduced, locally, to a constant slope. No time and clock synchronization errors were included in the analysis. However, their effects on FF-SAR performance could be simulated by the derived FF-SAR signal model by injecting the terms of the common and the spatial diversity arrays with various realizations of these errors. Similarly, even though presented results did not take into account errors in the knowledge of the relative positions among the receivers, one could compute beamforming weights using baseline vectors that are different from the simulated ones to model the accuracy of the relative positioning system. Future activities are planned towards the

generalization of the signal model and of the way simulations are carried out for representing error sources which may limit true FF-SAR imaging.

REFERENCES

[1] COSMO-SkyMed Web Site. Accessed: Jun. 14, 2019. [Online]. Available: http://www.cosmo-skymed.it/en/index.htm

[2] ESA Sentinel Online. Accessed: Jun. 14, 2019. [Online]. Available: https://sentinel.esa.int/web/sentinel/missions/sentinel-1

[3] G. Krieger et al, "TanDEM-X: a satellite formation for high-resolution SAR interferometry," IEEE Trans Geosci Remote Sens., Vol. 45, no. 11, pp. 3317–3341, Oct. 2007.

[4] G. Krieger et al., "TanDEM-X," in: M. D'Errico (ed.) Distributed Space Missions for Earth System Monitoring, Space Technology Library, Springer Science+Business Media New York, Vol. 31, pp. 387-436, 2013.

[5] TecSAR (SAR Technology Demonstration Satellite). Accessed: Ju. 14, 2019. [Online]. Available: https://directory.eoportal.org/web/eoportal/satellite-missions/t/tecsar

[6] RISAT-2 (Radar Imaging Satellite-2). Accessed: Jun. 14, 2019. [Online]. Available : https://directory.eoportal.org/web/eoportal/satellite-missions/r/risat-2

[7] ICEye Web Site. Accessed: Jun. 14, 2019. [Online]. Available: https://www.iceye.com/

[8] P. Gogineni et al., "A CubeSat Train for Radar Sounding and Imaging of Antarctic Ice Sheet," Proc. of IGARSS, pp. 4138-4141, July 2018.

[9] J. C. Curlander and R. N. McDonough, Synthetic Aperture Radar Systems and Signal Processing, 1st ed. New York, NJ, USA: Wiley, 1991.

[10] A. Moccia, "Synthetic aperture radar," in Encyclopedia of Aerospace Engineering, R. Blockley and W. Shyy, Eds. Chichester, U.K.: Wiley, Jun. 2012.

[11] P.A. Rosen, S. Hensley, I.R. Joughin, F.K. Li, S.N. Madsen, E. Rodriguez, R.M. Goldstein, "Synthetic aperture radar interferometry," Proc IEEE 88(3):333–382, 2000.

[12] P. Lopez-Dekker, G. Krieger, A. Moreira, "Multistatic Radar Systems," Distributed Space Missions for Earth System Monitoring M. D'Errico, Ed., New York, USA: Springer, 2013, pp. 61-122.

[13] N. Gebert, B. C. Dominguez, M. W. J. Davidson, M. D. Martin, P. Silvestrin, "SAOCOM-CS - A passive companion to SAOCOM for single-pass L-band SAR interferometry," in Proc. 10th EUSAR, Berlin, Germany, Jun. 2014.

[14] O. Montenbruck, R. Kahle, S. D'Amico, J.-S. Ardaens, Navigation and control of the TanDEM-X formation, The Journal of the Astronautical Sciences, Vol. 55, no. 3, pp. 341-357, Sep. 2008.

[15] G. Fasano, A. Renga, M. D'Errico, "Formation Geometries for Multistatic Sar Tomography," Acta Astronautica, Vol. 96, March–April 2014, pp. 11-22.

[16] G. Krieger, M. Younis, "Impact of oscillator noise in bistatic and multistatic SAR," IEEE Geosci. Remote Sens. Lett. Vol. 3, pp. 424-428, 2006.

[17] M. Younis, R. Metzig, G. Krieger, "Performance prediction of a phase synchronization link for bistatic SAR," IEEE Geosci. Remote Sens. Lett., Vol 3, pp. 429–433, 2006.

[18] N. Roth, B. Risi, C. Grant, R. Zee, "Flight results from the CanX-4 and CanX-5 formation flying mission," Proc. of the ESA Small Satellites, Systems & Services Symposium, Valletta, Malta, June 2016.

[19] S. Duque, C. Rossi, T. Fritz, "Single-Pass Tomography with Alternating Bistatic TanDEM-X Data," IEEE Geosci. Remote Sens. Lett., Vol. 12, no. 2, pp. 409-413, Aug. 2014

[20] S. Tebaldini, L. Ferro-Famil, "SAR tomography from bistatic single-pass interferometers," Proc. of IGARSS, Jul. 2017.

[21] S.V. Baumgartner, G. Krieger, "Dual-Platform Large Along-Track Baseline GMTI," IEEE Trans. Geosci. Remote Sens., Vol. 54, no. 3, pp. 1554-1574, Oct. 2015.

[22] R. C. Heimiller, "Theory and Evaluation of Gain Patterns of Synthetic Arrays," IRE Trans. On Military Electronics, Vol. MIL-6, No. 2, pp. 122-129, April 1962.

[23] T. Kraus, G. Krieger, M. Bachmann, A. Moreira, "Spaceborne Demonstration of Distributed SAR Imaging with TerraSAR-X and TanDEM-X," IEEE Geosci. Remote Sens. Lett., Vol. 16, No. 11, pp. 1731-1753, November 2019.

[24] V. K. Ithapu and A. K. Mishra, "Cooperative Multimonostatic SAR: A New SAR Configuration for Improved Resolution," IEEE Antennas Wirel. Propag. Lett., Vol. 9, pp. 701-704, July 2020.

[25] G. Krieger, N. Gebert, A. Moreira, Unambiguous SAR Signal Reconstruction from Nonuniform Displaced Phase Center Sampling, IEEE Geoscience and Remote Sensing Letters, Vol.1, Issue 4, pp. 260-264, 2004.

[26] N. Gebert, G. Krieger, A. Moreira, Digital Beamforming on Receive: Techniques and Optimization Strategies for High-Resolution Wide-Swath SAR Imaging, IEEE Trans. Aerosp. Electron. Sys., Vol. 45, No. 2, pp. 564-592, April 2009.

[27] N. A. Goodman, J. M. Stiles, "Resolution and Synthetic Aperture Characterization of Sparse Radar Arrays," IEEE Trans. Aerosp. Electron. Syst., Vol. 39, No. 3, pp. 921-935, Jul. 2003, DOI: 10.1109/TAES.2003.1238746.

[28] A. Goodman, "SAR and MTI Processing of Sparse Satellite Clusters," Ph.D. dissertation, Dept. Elect. Eng. and Computer Sci., Univ. of Kansas, 2002.

[29] H. Rott et al., "SESAME: A single-pass interferometric SEntinel-1 companion SAR mission for monitoring GEO- and biosphere dynamics," Proc. of IGARSS, pp. 107-110, Jul. 2017.

[30] P. Lopez-Dekker, "STEREOID: a multistatic extension of Sentinel-1 to observe land, ice, and ocean surface dynamics," ESA Conference on Bistatic and Multistatic SAR Systems and Applications, Delft, The Netherlands, 19-21 March 2019.

[31] J. Mittermayer, G. Krieger, M. Zonno, A. Bojarski, "Innovative MirrorSAR Concept for Multi-Static HRWS," ESA Conference on Bistatic and Multistatic SAR Systems and Applications, Delft, The Netherlands, 19-21 March 2019.

[32] T. Börner, P. López-Dekker, G. Krieger, M. Bachmann, A. Moreira, M. Hartmut, "Passive Interferometric Ocean Currents Observation Synthetic Aperture Radar (PICOSAR)." in Small Satellites for Earth Observation - Missions & Technologies, Operational Responsive Space, Commercial Constellations IAA Book Series, Vol. 1, no. 4, pp. 53-60, 2014.

[33] T. Sephton and A. Wishart, TOPOLEV and C-PARAS, , in: M. D'Errico (ed.) Distributed Space Missions for Earth System Monitoring, Space Technology Library, Springer Science+Business Media New York, Vol. 31, pp. 474-508, 2013.

[34] G. Krieger and A. Moreira, "Spaceborne bi- and multistatic SAR: Potential and challenges," Proc. Inst. Elect. Eng.—Radar, Sonar Navig., vol. 153, no. 3, pp. 184–198, Jun. 2006.

[35] A. Moccia, A. Renga, Bistatic Synthetic Aperture Radar, in M. D'Errico (ed.) Distributed Space Missions for Earth System Monitoring, Space Technology Library, 2013, Springer Science+Business Media New York, Vol. 31 pp. 3-59, 2013.

[36] M. Antoniou et al., Passive SAR Satellite Constellation for Near-Persistent Earth Observation: Prospects and Issues, IEEE Aerosp. Electron. Sys. Magazine, Vol. 33, o. 12, pp. 4-15, Dec. 2018.

[37] S. Sarno, M. D. Graziano, G. Fasano, M. D'Errico, Very-low altitude parasitic radar distributed on small satellites, Advances in Space Research, Vol. 62, pp. 3462–3474, Mar. 2018.

[38] I. G. Cumming and F. Wong, Digital Processing of Synthetic Aperture Radar. Norwood, MA: Artech House, 2005.

[39] W. Emery, A. Camps, Introduction to Satellite Remote Sensing. Amsterdam, Netherlands: Elsevier, 2017.

[40] T. C. Cheston, J. Frank, "Phased Array Radar Antennas," in Radar Handbook, M. I. Skolnik, Ed. 2nd ed. New York, NY, USA: McGraw-Hill, 1990, ch. 7.

[41] A. Moccia, A. Renga, "Spatial Resolution of Bistatic Synthetic Aperture Radar: Impact of Acquisition Geometry on Imaging Performance," IEEE Trans. Geosci. Remote Sens., vol. 49, no. 10, pp. 3487-3503, Oct. 2011, DOI 10.1109/TGRS.2011.2115250.

[42] G. P. Cardillo, "On the use of gradient to determine bistatic SAR resolution," in Proc. Antennas Propag. Soc. Int. Symp., vol. 2, pp. 1032–1035, 1990

[43] T. Zeng, M. Cherniakov, and T. Long, "Generalized approach to resolution analysis in BSAR," IEEE Trans. Aerosp. Electron. Syst., vol. 41, no. 2, pp. 461–474, Apr. 2005.

[44] H. L. Van Trees, "Arrays and Spatial Filters", in *Optimum Array Processing. Detection, Estimation and Modulation Theory, Part IV*, H. L. Van Trees, Ed., New York, USA: Wiley Interscience, 2002, pp. 17-77.

[45] M. Rodriguez-Cassola, P. Prats-Iraola, P. Lopez-Dekker, A. Reigber, G. Krieger, A. Moreira, "Autonomous time and phase calibration of spaceborne bistatic SAR systems," in: Proceedings of the European Conference on Synthetic Aperture Radar, EUSAR, June 2014, Berlin, Germany. pp. 264–267.

[46] M. D. Graziano, A. Renga, M. Grasso, A. Moccia, "PRF Selection in Formation-Flying SAR: Experimental Verification on Sentinel-1 Monostatic Repeat-Pass Data," *Remote Sens.*, 12, 18, https://doi.org/10.3390/rs12010029, 2019.

[47] R. Kroes, O. Montenbruck, W. Bertiger, P. Visser, P., "Precise GRACE Baseline Determination Using GPS," *GPS Solutions_*, Vol. 9, No. 1, April 2005, pp. 21–31.

[48] C. Gierull, "Bistatic synthetic aperture radar," Defence R&D Canada, Ottawa, ON, Canada, Tech. Rep. DRDC-OTTAWA-TR-2004-190, 2004.

[49] J. Homer, E. Donskoi, B. Mojarrabi, J. Palmer, and K. Kubik, "Three-dimensional bistatic synthetic aperture radar imaging system: Spatial resolution analysis*," Proc. Inst. Elect. Eng.-Radar Sonar Navig.*, vol. 152, no. 6, pp. 391–394, Dec. 2005.

[50] I. Walterscheid, J. Klare, A. R. Brenner, J. H. G. Ender, and O. Loffeld, "Challenges of a bistatic spaceborne/airborne SAR experiment," in *Proc. 6th EUSAR*, Dresden, Germany, May 2006.

[51] C. Cafforio, C. Prati, and F. Rocca, "SAR data focusing using seismic migration techniques," *IEEE Trans. Aerosp. Electron. Syst.*, vol. 27, no. 2, pp. 194-207, 1991, DOI: 10.1109/7.78293.

[52] C. Prati and F. Rocca, "Improving Slant-Range Resolution with Multiple SAR Surveys," *IEEE Trans. Aerosp. Electron. Syst.*, vol. 29, no. 1, pp. 135-144, Jan. 1993, DOI 10.1109/7.249119.

[53] R. Bamler, P. Hartl, "Synthetic aperture radar interferometry", *Inverse Problems*, vol. 14, R1-R54, Apr. 1998.

[54] D. Massonnet, "Capabilities and Limitations of the Interferometric Cartwheel," *IEEE Trans. Geosci. Remote Sens.*, vol. 39, vo. 3, pp. 506-520, Mar. 2001, DOI: 10.1109/36.911109.

[55] F. K. Li and W. T. K. Johnson, "Ambiguities in spaceborne synthetic aperture radar systems," *IEEE Trans. Aerosp. Electron. Syst.,* vol. AES-19, no. 3, pp. 389–397, May 1983.

[56] R. Opromolla, G. Fasano, G. Rufino, M, Grassi, "Design of relative trajectories for in orbit proximity operations", Acta Astronaut. Vol. 145, pp. 342–356, 2018.

[57] M. Antoniou, A. G. Stove, A. Sayin, G. Atkinson, M. Cherniakov, H. Ma, H. Kuschel, D. Cristallini, P. Wojaczek, Craig I. Underwood, A. Moccia, A. Renga, G. Fasano, "Passive SAR Satellite Constellation for Near-Persistent Earth Observation: Prospects and Issues," *IEEE Aerosp. Electron. Syst. Mag.*, Vol. 33, No. 12, pp. 4-15, Dec. 2018, DOI: 10.1109/MAES.2018.170178.

Alfredo Renga (M'19) was born in Caserta, Italy, in 1981. He received the M.S. degree *(cum laude)* in aerospace engineering and the Ph.D. degree in industrial engineering from the University of Naples Federico II, Naples, Italy, in 2006 and 2010, respectively. His research interests include spaceborne distributed synthetic aperture radar (SAR), Moon-based SAR, maritime sea traffic monitoring by monostatic and bistatic SAR data, radar-based navigation od small UAVs, and differential global positioning system techniques for accurate relative navigation of aerospace platforms.

He an Associate Professor of Aerospace Systems and a Lecturer of aerospace remote sensing systems and space mission design with the School of Engineering, Naples, Italy. His scientific production includes more than 100 scientific papers (since 2007) published in distinguished international journals, conference proceedings, and book chapters, and frequently referenced in the literature. He held contracts and carried out research activities with the Second University of Naples, Naples, the University of Naples Parthenope, Naples, and CO.RI.S.T.A., Naples, a private research consortium on advanced remote sensing systems led by Thales Alenia Space Italy.

He has been the Scientific Responsible of several research projects funded or supported by national and international institutions (ASI, DLR).

Maria Daniela Graziano received the B.S. and M.S. degrees (*cum laude*) in aerospace engineering and the Ph.D. degree in aerospace science and technology from the Second University of Naples, Naples, Italy, in 2005, 2008, and 2011, respectively. She is currently an Assistant Professor and Lecturer of Space Systems and Aerospace Program Management with the Department of Industrial Engineering of the University of Naples "Federico II". Her research interests include satellite constellation analysis and design, mission design for EO missions, distributed synthetic aperture radar (SAR), maritime sea traffic monitoring by SAR data processing. She has been involved in several research projects funded by national and international institutions (ASI, ESA, Ministry of Defence) and her scientific production included more than 50 scientific papers published in distinguished international journals, conference proceedings, and book chapters, and frequently referenced in the literature.

Antonio Moccia (SM'09) has been a Staff Scientist since 1983 and a Professor of aerospace systems since 1990 with the School of Engineering, University of Naples, Italy. His research interests include aerospace high-resolution remote sensing systems mission analysis, design, and data processing, and aerospace systems dynamics, guidance, navigation, and control. Since 1975, he has held grants and contracts from private and public industries and institutions in his research fields.

He has authored or co-authored over 200 scientific papers. He has been an Invited Speaker and a Lecturer of international conferences and courses. He is a reviewer for international journals and of research proposals issued by national and international authorities.

Prof. Moccia is a member of the national and international committees and working groups and a Principal or Co-Investigator of several national and international research programs. He is member of the ORFEO Committee for Italian–French cooperation on space remote sensing as a representative of the Italian Ministry for Research from 2002 to 2012, a member of the Scientific Consulting Committee of the Italian Aerospace Research Center from 2010 to 2012, and a Co-Chair of the International Astronautical Federation International Program Committee from 2010 to 2012. Since 2019 he is the Scientific Coordinator of the Aerotech Academy, a joint project between Leonardo S.p.A. and University of Naples Federico II for advanced, post-graduated, interdisciplinary training in aerospace engineering and in 2020 he was appointed member of the Mission Advisory Group of the Italian Space Agency PLATINUM-1 mission and coordinator of the Aerospace Sector of the Commission of Experts appointed by the Italian Ministry of University and Research for the National Research Plan 2021-2027.